Materials Advances

ROYAL SOCIETY OF CHEMISTRY

PAPER

View Article Online
View Journal | View Issue

Cite this: *Mater. Adv.*, 2025, 6, 2654

Synthesis of TiO_2–CuO@graphene oxide hybrid bionanocomposite with enhanced antibacterial and organic dye degradation activities†

Basma A. Omran, ‡*[ab] M. O. Abdel-Salam, ‡[cd] Hebatullah H. Farghal, [e] Mayyada M. H. El-Sayed *[e] and Kwang-Hyun Baek*[b]

The cumulative spread of infectious diseases and water pollution necessitates the development of innovative green materials. To address this challenge, titanium oxide (TiO_2) and copper oxide (CuO) nanoparticles (NPs) were mycofabricated using *Trichoderma virens* filtrate, which was grafted with graphene oxide (GO) nanosheets prepared *via* the modified Tour's method, resulting in a TiO_2–CuO@GO bionanocomposite. XRD revealed peaks corresponding to hexagonal carbon, rutile tetragonal TiO_2, and tenorite monoclinic CuO in the TiO_2–CuO@GO, having average crystallite sizes of 10.65 and 25.73 nm for GO and TiO_2–CuO@GO, respectively. FTIR revealed distinct absorption bands corresponding to oxygen-containing functional groups such as –OH, C=O, C=C, and C–OH. EDX spectra confirmed homogenous elemental distributions of Ti 2p, Cu 2p, O 1s, and C 1s in the bionanocomposite. The zeta potential values and hydrodynamic sizes were −36.8 mV and 291.1 nm for GO and +25.6 mV and 603.2 nm for TiO_2–CuO@GO, respectively. FE-SEM and HRTEM revealed that GO displayed a transparent, flaky structure with few wrinkles, whereas TiO_2–CuO@GO displayed opaque, rounded TiO_2 NPs and elongated, rod-shaped CuO NPs loaded onto GO. The bionanocomposite exhibited potent antibacterial activity against various foodborne and phytobacterial pathogens. TiO_2–CuO@GO was evaluated as a nanocatalyst for the degradation of Congo red at initial concentrations ranging from 10 to 50 mg L^{-1}. Upon activation with peroxymonosulfate, the material demonstrated a degradation efficiency of 70% within 28 min. Enhanced dye removal under saline conditions indicated the improved efficiency of the nanocatalyst. This study highlights the multidisciplinary potential of TiO_2–CuO@GO for applications in food packaging, agriculture, and wastewater treatment.

Received 11th January 2025,
Accepted 23rd March 2025

DOI: 10.1039/d5ma00031a

rsc.li/materials-advances

1. Introduction

The interconnection between phytopathogens, foodborne pathogens, and organic dye pollutants influences ecosystem integrity, agricultural productivity, food safety, and water quality.[1] Their combined effects are deeply intertwined, contributing to environmental pollution, affecting ecosystem stability, threatening crop yields, and increasing risks to human health. Their collective impact is evident in soil degradation, water contamination, and food safety risks.[2] Foodborne pathogens pose severe risks to public health and food safety, presenting a major global concern. More than 250 foodborne diseases are attributed to pathogenic microorganisms found in food. Amongst, foodborne bacterial pathogens represent the second most common causative agents of foodborne diseases.[3] In the United States, foodborne pathogens are responsible for approximately 9.4 million cases of foodborne diseases, whereas in England and Wales, they are responsible for 1.7 million cases.[4] This proportion is even higher in developing countries, where foodborne pathogens severely threaten public health. In addition to foodborne pathogens, plant diseases caused by phytopathogens represent a major concern, posing serious threats to plant health and agricultural production, thus resulting in substantial economic losses and ecological damage.[5] Over time, the incidence and severity of bacterial plant diseases have increased owing to global climate change and shifting agricultural patterns.[6] Bacterial phytopathogens are

[a] *Department of Processes Design & Development, Egyptian Petroleum Research Institute (EPRI), Nasr City, Cairo 11727, Egypt. E-mail: obasma@ynu.ac.kr*
[b] *Department of Biotechnology, Yeungnam University, Gyeongbuk, Gyeongsan 38541, Republic of Korea. E-mail: khbaek@ynu.ac.kr*
[c] *Analysis and Evaluation Department, Egyptian Petroleum Research Institute, Nasr City, Cairo 11727, Egypt*
[d] *Central Analytical laboratories, Egyptian Petroleum Research Institute, Nasr City, Cairo 11727, Egypt*
[e] *Department of Chemistry, School of Sciences and Engineering, The American University in Cairo, New Cairo 11835, Egypt. E-mail: mayyada@aucegypt.edu*
† Electronic supplementary information (ESI) available. See DOI: https://doi.org/10.1039/d5ma00031a
‡ These authors contributed equally to the work.

highly adaptable microorganisms. They possess resilient traits that enable them to survive and thrive in harsh conditions. These pathogens can spread quickly when environmental conditions become favorable. Factors such as high humidity, warm temperatures, and heavy rainfall contribute to their rapid proliferation. These bacteria infect plants by penetrating through their natural openings or wounds.[7] Common diseases caused by these phytopathogens include bacterial wilt, blight, canker, and soft rot, which affect various crops such as tomatoes, potatoes, and citrus fruits.[8,9] Plants infected by these phytopathogens exhibit various symptoms, such as stunted growth, wilting, leaf spots, and fruit rot. This leads to a reduction in the quantity and quality of crop yield and in some cases, complete crop failure. The economic impacts of such infestations on farmers can be profound owing to reduced quantities of marketable crops, increased costs associated with disease management, and potential trade restrictions on the affected agricultural products. Synthetic pesticides, including fungicides, bactericides, and herbicides, are commonly used to combat phytopathogens.[10] Although these chemicals offer benefits such as rapid action, reliability, and high effectiveness, they have some limitations such as adverse effects on human health, environment, and non-target microorganisms. Furthermore, they can contribute to the development of resistance and resurgence in various pathogens and pests.[11–13] Hence, combating foodborne pathogens and bacterial phytopathogens is crucial for maintaining sustainable food production and ensuring healthy crop yield.[14]

Another major global challenge is the discharge of industrial effluents, particularly those containing dyes, into water bodies. In general, effluents discharged from industries such as textiles, leather, pulp, paper, synthetic fibers, and plastics contain a complex mixture of synthetic dyes and other hazardous chemicals.[15] These pollutants adversely affect aquatic ecosystems, human health, and the environment. The accumulation of dye-containing effluents leads to water discoloration, increased biochemical and chemical oxygen demands, toxicity to aquatic organisms, bioaccumulation in the food chain, and soil contamination.[16] Furthermore, synthetic dyes exhibit complex chemical structures and are resistant to degradation. These dyes remain stable under various environmental conditions, which complicates their degradation in traditional wastewater treatment facilities. Azo dyes, for instance, comprise chromophores linked to benzenic and/or naphthalenic rings.[17] Although Congo red (CR) has several useful properties, such as amyloid detection, staining specificity, and *in vivo* visualization, it is a highly toxic dye with carcinogenic effects.[18]

Traditional wastewater treatment methods include adsorption,[19] flocculation/coagulation,[20] biological treatments,[21] ion exchange.[22] and membrane technologies.[23] However, these methods have several limitations, including high operational costs, incomplete removal of contaminants and metals, generation of secondary pollutants and byproducts that become more toxic over time, production of toxic sludge, susceptibility to fouling, and low overall efficiency.[24] Advanced oxidation processes (AOPs) offer a more effective solution by generating highly reactive species capable of degrading organic pollutants in water and wastewater.[25] Potassium peroxymonosulfate (PMS), a potent oxidizing agent, is widely used in AOPs. It generates highly reactive sulfate radicals, which are particularly effective in disintegrating the chains of contaminants.[26]

Graphene-based materials, particularly graphene oxide (GO), are utilized as reinforcing materials for the synthesis of composites owing to their flexible, carbon flake structure.[27] GO features a honeycomb-like arrangement of carbon atoms with abundant oxygen-containing functional groups. It has gained prominence as an advanced nanocarrier, especially for antimicrobial and catalytic applications. Compared to other carbon-based nanomaterials (NMs) like carbon nanotubes, fullerenes, and activated carbon, GO exhibits several unique advantages, including a large surface area, excellent thermal stability and conductivity, high mechanical strength and toughness, superior electrical conductivity, and an abundance of oxygen-containing functionalities. Additionally, GO offers cost-effectiveness, scalability, enhanced pollutant adsorption capacity, and improved antibacterial and antifungal properties.[28] However, modifying GO network with metal-based nanoparticles (NPs) endows the resulting nanocomposites with properties that are superior to those of the individual components.[29,30] Titanium dioxide (TiO_2) NPs are extensively utilized as highly efficient photocatalysts in water and wastewater treatment applications owing to their high oxidation potential, broad-spectrum activity, stability, cost-effectiveness, low toxicity, and scalability.[31] When incorporated into composite structures, TiO_2 NPs can further enhance the structural properties and functionalities of the materials.[32] Copper oxide (CuO) NPs exhibit unique physicochemical features, along with low toxicity and cost-effectiveness. Moreover, they combat various pathogenic microorganisms, possess antioxidant and anticancer potential, and demonstrate photocatalytic activity, making them ideal candidates for environmental remediation.[33–35]

The green synthesis of NMs is an environmentally friendly and a sustainable approach that is reliant on natural biological resources. This approach significantly minimizes or entirely avoids the use of harmful chemicals, making it a safer alternative for the environment. It also minimizes waste production, promotes material reuse, and lowers energy consumption. Furthermore, it is cost-effective and can be scaled up efficiently. Various natural biological entities—including plant extracts, agricultural byproducts, microorganisms (*e.g.*, bacteria, yeast, fungi, and actinomycetes), algae, and biomolecules—serve as mediators in NM synthesis.[36–38] A recent review conducted by Rana *et al.*[39] revealed that plant-derived NPs were the most extensively researched, accounting for 40% of the studies conducted on the biological synthesis of NMs. This was followed by bacterial-mediated synthesis at 34%, biomolecule-based synthesis at 15%, fungi-based synthesis at 7%, and algae-based synthesis at 4%. The synthesis of nanobiomaterials adheres to the twelve core principles of green chemistry. These principles focus on preventing waste and improving atom economy. They advocate for the use of less hazardous synthesis methods and the design of safer chemicals and solvents. Energy efficiency is prioritized, along with the utilization of renewable feedstocks. Byproducts are minimized, and catalysts with high selectivity are favored over stoichiometric reagents. The process emphasizes the release of degradable products and

incorporates real-time analysis to avoid pollution. Additionally, inherently safe processes are adopted to reduce any risks.[40]

Fungi possess distinctive merits compared to other biological systems (bacteria, plants, *etc.*), involving (i) large surface area of fungal mycelia; endowing fungi as proficient metal ion biosorbents and facilitating their reduction to metal NPs, (ii) better polydispersity, stable structures, and diversity in the dimensions of the produced NPs; (iii) secretion of an array of bioactive secondary metabolites and enzymes that mediate nanoparticle synthesis; and (iv) cost-effectiveness due to the higher biomass.[41,42] Several fungal species have notably advanced the green synthesis of NMs, including *Verticillium* sp.,[43] *Pycnoporus* sp.,[44] *Sclerotinia* sp.,[45] *Trichoderma* sp.,[46] *Aspergillus* sp.,[7] and *Fusarium* sp.[47] The mycogenic synthesis of NMs has been facilitated by the diverse secondary metabolites produced by these fungi, which play crucial roles in NM production. *Trichoderma* sp., in particular, are plant symbionts that establish mutualistic endophytic relationships with a wide variety of plant species.[48] Their economic significance spans various fields, such as agriculture, bioremediation, biotechnology, and, more recently, nanotechnology.[49,50] *Trichoderma* sp. are known for their rapid growth ability; biocontrol activity; and high secretion potential for enzymes, antibiotics, and secondary metabolites. These fungal species are widely utilized in biotechnological applications, such as bioremediation, production of enzymes, and development of products that enhance plant growth and biological control.[51] Among these species, *Trichoderma virens*, an endophytic fungus, which is characterized by the production of bioactive compounds and secondary metabolites such as pyrones, peptaibols, polyketides, non-ribosomal peptides, and terpenes.[52–54] The selection of *T. virens* was based on its exceptional enzymatic potential such as production of reductases, and the secretion of extracellular proteins, carbohydrates, and compounds with antibiotic activity, which play a pivotal role in mediating the synthesis of NMs. In our previous studies, *T. virens* exhibited high efficiency in mediating the mycogenic synthesis of single metallic NPs,[55] as well as bimetallic NPs, such as Ag_2O/TiO_2[56] and Ag_2O/CuO.[57] Notably, to date, only one study has documented the preparation of a CuO–TiO_2 composite *via* a sol–gel technique, followed by its anchoring onto GO through a hydrothermal process. This chemically synthesized composite was then evaluated for its photocatalytic potential in degrading bisphenol A.[31] The combination of TiO_2, CuO, and GO in this study was carefully selected based on their synergistic and complementary characteristics. The rationale for selecting TiO_2–CuO@GO was the enhanced catalytic efficiency, synergistic antimicrobial activity, improved pollutant adsorption and degradation. This strategic combination offers a more effective, sustainable, and cost-efficient solution for antimicrobial applications and wastewater treatment.

This study seeks to tackle the aforementioned interconnected environmental challenges by developing an innovative material with multifunctional capabilities. The approach focuses on enhancing food safety, promoting sustainable agriculture, and ensuring a cleaner environment, emphasizing the critical link between human health, agriculture, and environmental sustainability. It offers unique insights into the biological synthesis of a TiO_2–CuO@GO bionanocomposite using *T. virens*, contributing to the existing knowledge and addressing current research gaps. It also emphasizes the distinctive role of fungi as natural mediators in the synthesis of hybrid bionanocomposites. The optical, physicochemical, structural, and morphological properties of the as-prepared bionanocomposite are analyzed using various techniques. Furthermore, the practical applications of TiO_2–CuO@GO are assessed, including its biocidal potential against foodborne bacterial pathogens and phytopathogens, as well as its catalytic activity in the degradation of a polluting dye assisted by PMS.

2. Materials and methods

2.1. Chemicals

The graphite powder (99.9%, ultra "F" purity) used for GO preparation was sourced from Alfa Aesar (Haverhill, Massachusetts, United States). Meanwhile, potassium permanganate ($KMnO_4$), hydrochloric acid (HCl), phosphoric acid (H_3PO_4, 85%), sulfuric acid (H_2SO_4, 98%), and hydrogen peroxide (H_2O_2, 30%) were procured from Duksan Pure Chemicals Co., Ltd, Republic of Korea. Two precursor metal salts, namely copper(II) sulfate pentahydrate ($CuSO_4{\cdot}5H_2O$) and rutile titanium(IV) oxide (TiO_2), were used in the synthesis of the TiO_2–CuO@GO bionanocomposite. Anhydrous ethylene glycol was used to ensure a uniform and homogenous dispersion. CR dye and potassium peroxymonosulfate ($KHSO_5$) were employed in catalytic degradation experiments. All the aforementioned chemicals were purchased from Loba Chemie Pvt. Ltd (Mumbai, Maharashtra, India) or Sigma-Aldrich (St. Louis, MO, USA) and were of 99% analytical grade purity.

2.2. Preparation of GO nanosheets

Various methods have been reported for synthesizing GO, including the improved/modified Tour's method.[58–61] This method was employed in this study for GO synthesis *via* the oxidation of natural graphite powder (Fig. 1). Briefly, 2 g of graphite powder were added to a 9 : 1 mixture of concentrated H_2SO_4 and H_3PO_4 in a round-bottomed flask. The reaction mixture was cooled to a temperature between 0 °C and 5 °C in an ice bath. Subsequently, 12 g of $KMnO_4$ were gradually added to this mixture under continuous stirring while maintaining the same temperature. The reaction mixture was then removed from the ice bath and stirred continuously for 12 h at 50 °C. Then, the resulting mixture was returned to the ice bath, and deionized water was slowly added to terminate the reaction. Subsequently, 2 mL of H_2O_2 (30%) were added gradually to terminate the oxidation reaction, which was indicated by the appearance of a yellow paste, indicating a high level of oxidation. The reaction mixture was filtered using a Whatman filter paper and centrifuged at 10 000 rpm for 15 min to purify the product and remove residual salts and acids. The resulting colloidal paste was then washed repeatedly with deionized water, 30% HCl, and ethanol until the pH of the supernatant reached approximately 7, ensuring the complete removal of any residues. Finally, the residual solid was freeze–dried to obtain lamellar GO in a powder form for subsequent analyses and applications.

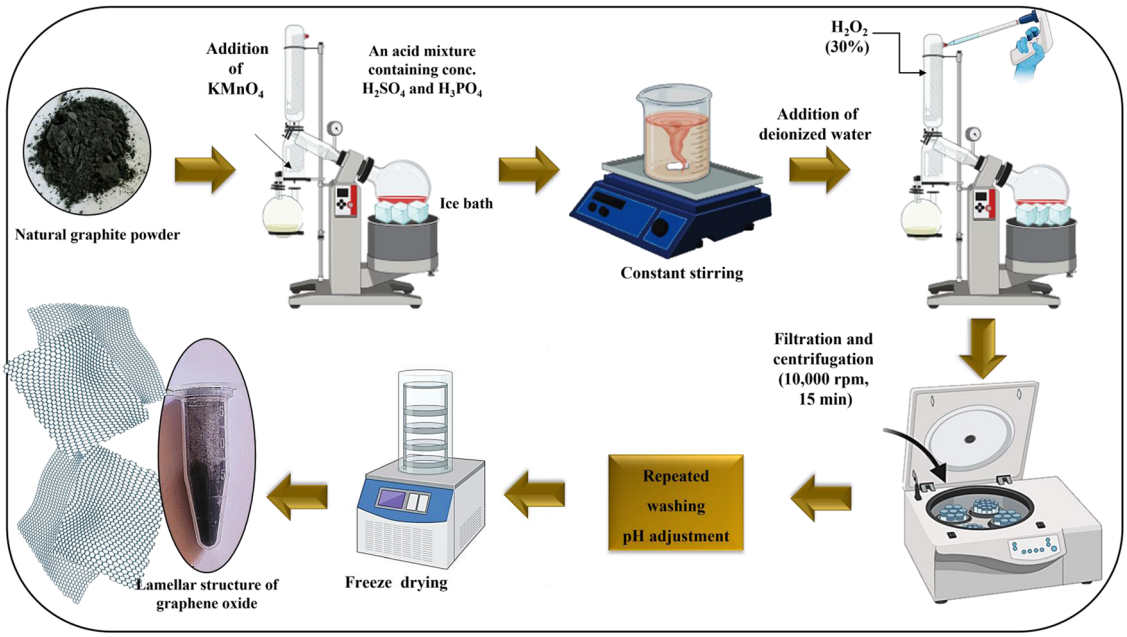

Fig. 1 Schematic representation showing the preparation of GO following modified Tour's method.

2.3. Mycogenic synthesis of TiO_2–CuO@GO

The fungus; *T. virens* (KACC 40800, Republic of Korea) was used to mediate the synthesis of TiO_2–CuO@GO. The cell-free fungal filtrate was prepared by following the methodology described by Omran *et al.*[62,63] The extracellular filtrate of *T. virens* exhibited a faint yellow color. Approximately 10 mg of GO were added to 50 mL of the extracellular fungal filtrate, after which the mixture was subjected to 15 min of sonication in a water bath ultrasonicator to ensure thorough and uniform dispersion. For the mycogenic synthesis of TiO_2–CuO@GO, two metal salt solutions—$CuSO_4{\cdot}5H_2O$ and TiO_2 (20 mM each)—were prepared and simultaneously added to the GO-fungal filtrate. The reaction mixture was then stirred for 30 min using a magnetic stirrer, and its pH was adjusted to an alkaline level (pH 9) using 5 mM NaOH. The suspension was then transferred to a shaking incubator and left overnight. During this period, the initial light-yellowish filtrate of *T. virens* gradually changed color and formed precipitates (Fig. 2). The resulting suspension was

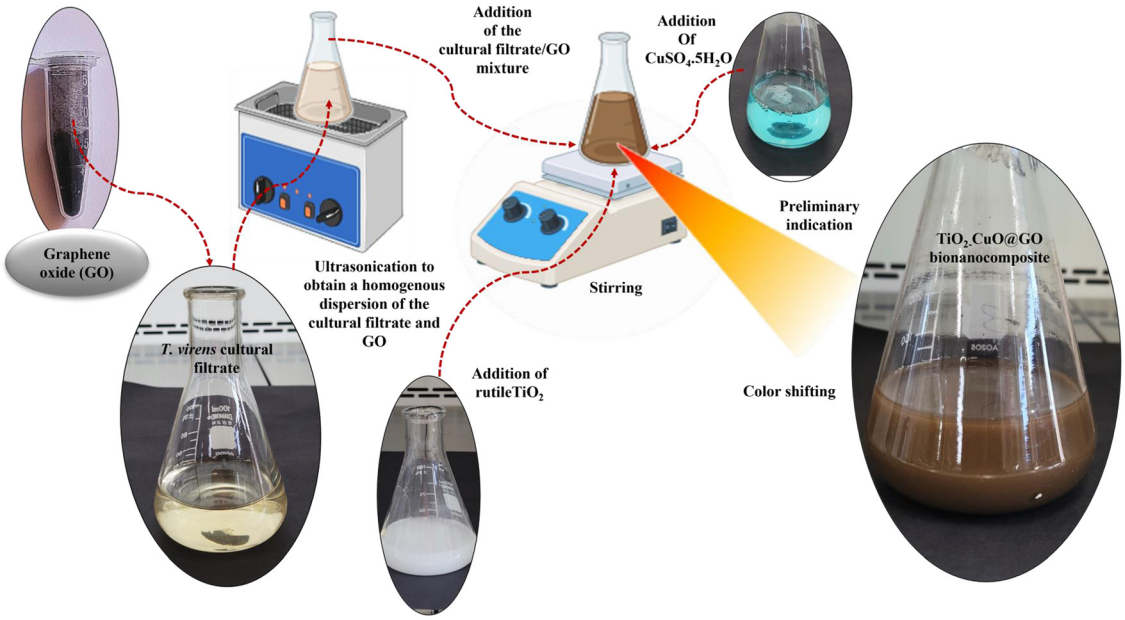

Fig. 2 A schematic diagram represents the mycogenic preparation process of the colloidal suspension containing TiO_2–CuO@GO bionanocomposite using *T. virens* cultural filtrate.

centrifuged at 7000 rpm for 10 min, and the precipitate was collected and washed thrice with double-distilled water and ethanol to eliminate impurities, organic residues, and excess reactants. The pre-washed precipitates were then dried in an oven at 60 °C overnight and stored for future use.

2.4. Characterization of GO and TiO_2–CuO@GO

The optical properties of GO and TiO_2–CuO@GO were examined by recording their absorption spectra in the ultraviolet-visible (UV/Vis) range (200–800 nm) using a UV/Vis diffuse reflectance spectrophotometer (Model-PerkinElmer Lambda 1050+ UV/Vis/NIR spectrophotometer, Waltham, Massachusetts, United States). The band gap energy (E_g) of the samples was calculated using a Tauc plot. To examine the interplanar spacing, crystal structure, and diffraction patterns of GO and TiO_2–CuO@GO, X-ray diffraction (XRD) was performed using a PANalytical X'PERT High Score diffractometer (Malvern, UK). XRD analysis was conducted at a scan rate of 0.02° min^{-1} across a 2θ range of 10°–80° using a CuKα radiation source (1.5406 Å). The recorded XRD data were compared with the diffraction peaks of crystalline materials documented in the database library of the Joint Committee on Powder Diffraction Standards-International Center for Diffraction Data (JCPDS-ICCD). A micro-Raman spectrometer (Horiba Scientific XploRA Plus, Osaka, Japan) was used to analyze the vibrational modes of GO and TiO_2–CuO@GO. A 532-nm laser excitation source was utilized, with a spectral resolution of 3 cm^{-1} and a spectrum acquisition duration of 100 s. The surface functionalization of GO and TiO_2–CuO@GO was evaluated using Fourier-transform infrared spectrophotometer (FTIR, Bio-Rad Excalibur Series FTS 3000, Bio-Rad, Hercules, California, USA). FTIR analysis was performed by blending the powdered synthesized samples with powdered anhydrous potassium bromide (KBr of FTIR grade) in a 1 : 100 ratio using a pelletizer. The FTIR spectra were recorded within a spectral range of 400–4000 cm^{-1} at a scan resolution of 4 cm^{-1}. Finally, X-ray photoelectron spectroscopy (XPS) was performed to determine the elemental composition and chemical oxidation states of GO and TiO_2–CuO@GO using a K-Alpha XPS machine (Thermo Fisher Scientific, Waltham, Massachusetts, USA). The recorded data were processed using Casa XPS software, and peak deconvolution was calculated using the Gaussian–Lorentzian equation.

Dynamic light scattering (DLS, a Nano ZS-S90 Malvern zeta potential analyzer, Worcestershire, UK) was performed to evaluate the average particle size distribution (in nm) and polydispersity index of GO and TiO_2–CuO@GO. A sample volume of 1 mL was utilized for each measurement, and the results were reported based on three independent replicates. Furthermore, a zeta potential analysis was conducted to determine the ionic surface charge and assess the colloidal stability of the synthesized samples. GO and TiO_2–CuO@GO were dispersed and diluted in anhydrous ethylene glycol, sonicated, and finally examined in glass cuvettes at a temperature of 25 °C. The surface morphologies and topographical structures of GO and TiO_2–CuO@GO were examined using field emission scanning electron microscopy (FE-SEM, Hitachi S-4800, Hitachi, Tokyo, Japan). Small quantities of the samples were mounted onto a stub using black conductive carbon tape. Then, the samples were coated with a 5-nm platinum layer *via* sputter coating. The samples were then examined at an operating voltage of 15 kV under high-vacuum conditions to achieve optimal resolution. The elemental distribution within the prepared bionanocomposite was analyzed on a per-area basis using an energy-dispersive X-ray (EDX) spectrophotometer equipped with a field emission scanning electron microscope. Additionally, the ultra-morphological nanoarchitecture of the prepared samples was confirmed through high-resolution transmission electron microscopy (HRTEM, JEOL-JEM 2100F, 80–200 kV, Tokyo, Japan). While triplicate measurements are essential for certain types of analyses, the consistency of the synthesis process, the nature of the techniques, and the complementary validation of results justified performing a single measurement for some of the characterization techniques in this study. Additionally, the results from each analysis were cross-validated using the employed complementary methods. All characterization techniques were conducted at the Core Research Support Center for Natural Products and Medical Materials at Yeungnam University, Republic of Korea.

2.5. Antibacterial activity assessment

2.5.1. Kirby–Bauer disc diffusion and microdilution assays. The antibacterial activities of the mycogenic TiO_2–CuO@GO bionanocomposite and GO were evaluated against foodborne bacterial pathogens, namely *Staphylococcus aureus* (ATCC 12600), *Escherichia coli* (ATCC 43889), and *Salmonella enterica Serovar Typhimuri*um (ATCC 14028), and other bacterial phytopathogens, namely *Clavibacter michiganensis* subsp. *michiganensis* (*Cmm*, KACC 17003), *C. michiganensis* subsp. *capsici* (*Cmc*, KACC 18448), wild-types and streptomycin-resistant mutants of *Pectobacterium carotovorum* subsp. *carotovorum* (*Pcc*), and *Xanthomonas citri* pv. *citri* (*Xcc*). The antimicrobial efficacies of GO and TiO_2–CuO@GO were assessed using the Kirby–Bauer disc diffusion assay, following the methodology outlined.[55–57] The antibacterial activity assessment included standard controls for comparison: streptomycin (at concentrations of 0.5 and 1 mg mL^{-1}) was used as a positive control, while ethylene glycol, which served as the dispersion medium for the synthesized bionanocomposite, was employed as a negative control. Furthermore, the minimum inhibitory concentration (MIC) and minimum bactericidal concentration (MBC) of TiO_2–CuO@GO against the tested bacterial pathogens were determined using the broth microdilution assay, as described by Omran *et al.*[62,63]

2.6. Catalytic degradation activity of TiO_2–CuO@GO

The catalytic performance of TiO_2–CuO@GO, prepared at varying concentrations (10–50 mg L^{-1}), was evaluated by adding 10 mg of the bionanocomposite and 80 mg of PMS to a 100 mL CR dye solution. The catalytic degradation of the dye solution at an initial concentration of 20 mg L^{-1} was assessed in the presence of NaCl (1.5 and 3%). Samples were extracted every 4 min and added to vials containing sodium thiosulfate pentahydrate (0.5 M) to terminate the catalytic reaction. The absorbance of the CR dye was then measured using a UV/VIS spectrophotometer at the

maximum wavelength (λ_{max}) of 497 nm. The remaining concentration of CR was calculated by plotting the obtained absorbance values on a calibration curve. Thereafter, the degradation efficiency was determined using the following equation:

$$\text{Degradation efficiency}\ (\%) = \frac{C_i - C_f}{C_i} \times 100 \qquad (1)$$

where C_i denotes the initial concentration of the CR dye, and C_f represents its remaining concentration after catalytic degradation.

2.7. Statistical analysis

The data reported in this study are expressed as the mean ± standard deviation. The results obtained from three independent replicates were analyzed using GraphPad Prism Software (Boston, MA, USA). Differences among groups were determined using a two-way repeated measures analysis of variance test. Statistical significance was defined at a probability value (p)-value of less than 0.0001.

3. Results and discussion

3.1. Mycogenic synthesis of TiO_2–CuO@GO

The oxidation of graphite using acids and oxidizing agents introduces oxygen-containing functional groups (such as hydroxyl, epoxy, carbonyl, and carboxyl) onto the graphene lattice, particularly at its edges and on its surface, thereby modifying the electronic structure of graphene and converting it into GO. Fungi play a pivotal role in the synthesis of NMs through a process known as mycosynthesis or mycogenic synthesis. This environmentally friendly approach offers notable benefits over other biological methods, including cost-effectiveness, biocompatibility, and ease of scalability. The mycogenic synthesis process involves several critical factors, including high fungal tolerance to metal ions; biomineralization and bioaccumulation capabilities; efficient metabolic activity; enzyme secretion capacity; interactions with peptides and proteins; and the large mycelial surface area, which kinetically promotes the nucleation of metal ions.[64,65]

Trichoderma spp. (Ascomycota, teleomorph: Hypocrea) are predominantly isolated from decaying organic matter and rhizosphere soil. This genus is highly adaptable to diverse ecological niches and is commonly found in different types of soils, as well as root and foliar environments. These environmentally friendly fungi play a critical role in sustainable agriculture by serving as commercially available microbial control agents against phytopathogens, promoting plant growth, improving soil health, and boosting stress tolerance.[66] Various metabolites, including terpenoids, cyclopeptides, diketopiperazines, alkaloids, polyketide, and other nitrogen-containing compounds, have been extracted from *Trichoderma* sp., all of which display diverse biological activities.[67] These metabolites interact with the targeted metal ions (*i.e.*, Ti^{4+} and Cu^{2+}) through several mechanisms, including biosorption and metal ion reduction, bioaccumulation and compartmentalization, metal chelation, stabilization of the produced nanostructures, nucleation and growth, and finally assembly on GO surface.[68,69] Tour's method was selected over other oxidative approaches due to its superior oxidation efficacy, enhanced dispersibility, improved material functionalization, higher degree of graphitization, scalability, control over temperature, and reduced emissions of harmful gases.[70,71] However, it has certain limitations, including reliance on specific precursor materials, structural defects, and extensive use of acids, raising environmental and safety concerns. Nanocomposites comprising two or more distinct types of NMs are gaining traction as innovative, multifunctional nanoformulations. These composites combine the unique properties of their individual components, offering advantages such as improved properties and biocompatibility, synergistic effects, enhanced stability, tailored multifunctionality, and economic efficiency.[62,72] The successful synthesis of TiO_2–CuO@GO was initially confirmed by the color change of *T. virens* filtrate, from a faint yellowish color to a dark brownish colloidal suspension. This colloidal dispersion was then centrifuged, and the resulting precipitate was washed, dried, and powdered for further analysis.

3.2. Physicochemical, structural, and morphological characteristics of GO and TiO_2–CuO@GO

UV/Vis absorption spectroscopy is a valuable tool for assessing the electronic and optical properties of materials. The GO sample displayed a characteristic absorption band near 230 nm, attributed to π–π* transitions in its aromatic C═C and C–C bonds, indicating strong UV absorption (Fig. 3a). Furthermore, a bump/shoulder band was observed at approximately 315 nm, which could be attributed to n–π* transitions.[73] Previous studies conducted by Kiani *et al.*[74] and Muqoyyanah *et al.*[75] have reported similar shoulder peaks at approximately 301 and approximately 303 nm, respectively. This absorption behavior could be attributed to electronic transitions within the material. Generally, in materials with a conjugated π system, π–π* electronic transitions occur owing to the overlap of adjacent p orbitals, creating delocalized π molecular orbitals. In these materials, UV or visible light absorption causes an electron transfer from the π-bonding molecular orbital to excite the corresponding π* anti-bonding molecular orbital. In GO, this π–π* transition is related to the delocalization of the π-bonding network within the graphene lattice.[76] The n–π* electronic transition involves electron excitation from a nonbonding or lone pair orbital (n) to the antibonding π* orbital.

In this study, the optical band gap energy (E_g) was evaluated using the Tauc plot method.[77] The equation for this Tauc plot is presented in eqn (2):

$$(\alpha h\nu)^n = A(h\nu - E_g) \qquad (2)$$

where α denotes the absorption coefficient, $h\nu$ represents the incident photon energy, n indicates an exponent dependent on the type of electronic transition (*e.g.*, $n = 1/2$ and $n = 2$ for direct and indirect allowed transitions, respectively), A denotes a proportionality constant, and E_g represents the optical band gap energy.[78] The Tauc plot was generated by plotting $(\alpha h\nu)^n$ against $h\nu$, and the linear section of the plot was extrapolated to yield the value of E_g. The GO and TiO_2–CuO@GO samples exhibited indirect allowed transitions, and the E_g value of GO was estimated to be 2.68 eV using the Tauc plot (Fig. 3b). This band gap energy of 2.68 eV is quite large, classifying GO as a

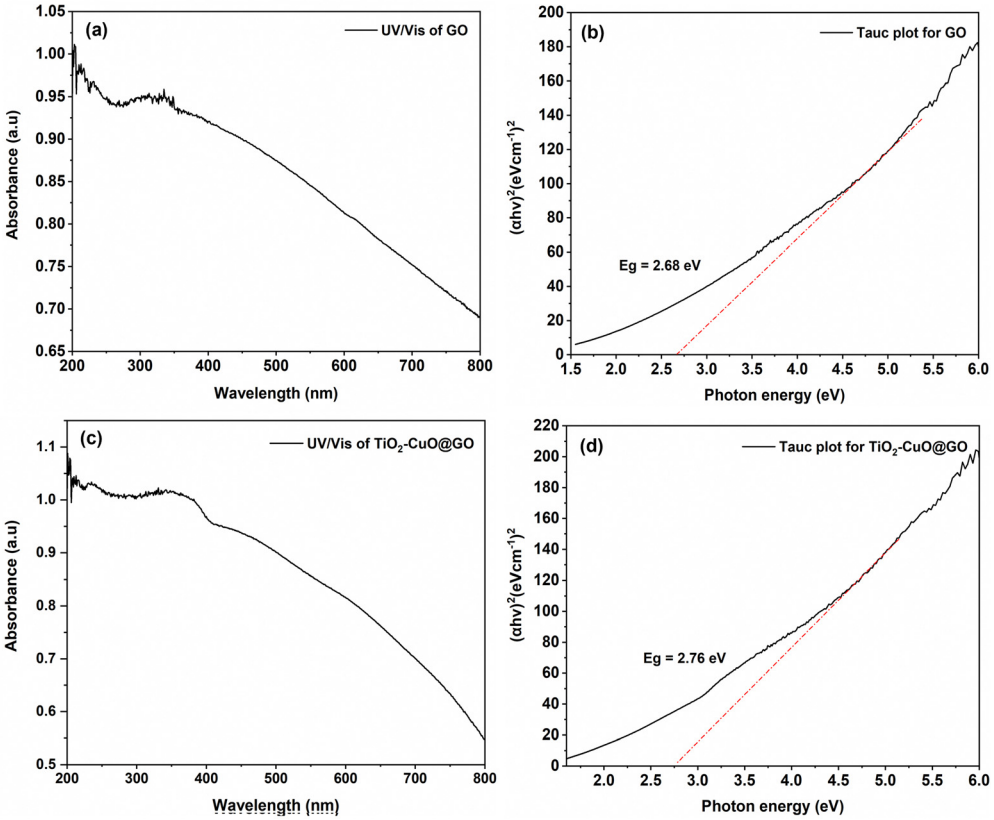

Fig. 3 UV-Vis spectra (a) and (c) and Tauc plot band gap energy (E_g) (b) and (d) of GO nanosheets and TiO_2–CuO@GO bionanocomposite, respectively.

wide bandgap semiconductor suitable for electronic and optoelectronic applications, where interactions with UV light are crucial. The TiO_2–CuO@GO bionanocomposite displayed absorption band edges at approximately 232, 361, and 422 nm, corresponding to GO, CuO, and TiO_2, respectively (Fig. 3c). The E_g value of this bionanocomposite was 2.76 eV, similar to that of a CuO–graphene–TiO_2 composite synthesized using a self-assembly method.[79] Notably, the change in E_g from 2.68 eV for GO to 2.76 eV for the prepared nanocomposite (Fig. 3d) is attributed to the introduction of additional energy levels below and above the conduction and valence bands, resulting in a higher concentration of oxygen vacancies. This change in energy levels could explain the observed red shift. The optical properties of the bionanocomposite were visibly evident in the color shift from a light yellowish color to a dark brownish color. This transformation could be attributed to the rearrangement of the crystalline structure, which reduced strain or static structural disorder.

The crystallographic phases of GO and TiO_2–CuO@GO were examined using XRD analysis across diffraction angles (2θ) ranging from 10° to 80° (Fig. 4a). GO exhibited a prominent broad diffraction peak at $2\theta = 10.96°$, corresponding to the (001) crystal plane of the crystalline structure of GO. Notably, this peak is associated with the presence of hydrophilic oxygen-containing functional groups formed within the basal planes of GO.[80] A similar peak position for GO was reported by Al-Gaashani *et al.*[81] The XRD pattern of TiO_2–CuO@GO displayed reflection peaks corresponding to the phases of rutile tetragonal TiO_2 (*P*42/*mnm*, 136; JCPDS card no. 01-077-0441) and tenorite monoclinic CuO (*C*2/*c*, 15; JCPDS card no. 00-041-0254). The diffraction peaks of the bionanocomposite were observed at 2θ angles of 8.21°, 25.39°, 27.46°, 35.55°, 36.11°, 38.71°, 41.27°, 44.04°, 54.27°, 56.70°, 57.27°, 62.66°, 64.08°, 68.18°, 68.93°, 69.82°, and 76.59°. The mean crystallite sizes of GO and TiO_2–CuO@GO were calculated using the Debye–Scherer's equation:

$$D = (K\lambda)/(\beta \cos\theta), \quad (3)$$

where D denotes the crystallite size, K represents the Scherer's constant (with a value of 0.94), λ denotes the X-ray wavelength (with a value of 0.154178 nm), β represents the full width at half maximum of the diffraction peaks, and θ represents Bragg's diffraction angle. The calculated average crystallite sizes for the as-prepared GO and TiO_2–CuO@GO samples were 10.65 and 25.41 nm, respectively. The XRD crystallographic data of these samples are detailed in Table S1 (ESI†). The sharp, high-intensity diffraction peaks observed in the XRD profile of TiO_2–CuO@GO confirmed the high crystallinity of the synthesized bionanocomposite.

Raman spectroscopy, which helps identify ordered or disordered crystalline structures of carbon materials, was performed to assess the level of disorder and defects present in the as-prepared materials.[82] The Raman spectra of GO and TiO_2–CuO@GO (Fig. 4b) displayed two dominant peaks; D and G bands. For GO, the D and G bands were observed at 1364.61 and 1617.72 cm^{-1}, respectively, with a 2D band centered at

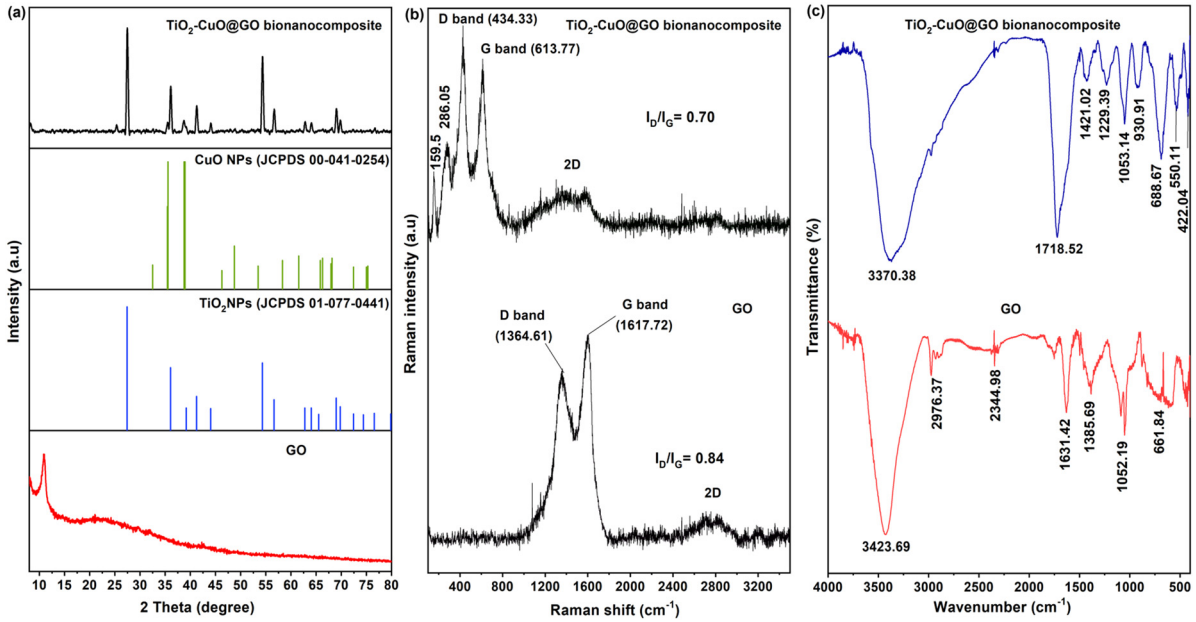

Fig. 4 XRD diffraction patterns (a), Raman spectra (b), and FTIR spectra (c) of GO and the mycogenic TiO_2–CuO@GO bionanocomposite.

2748.22 cm^{-1}. Whereas, the Raman spectrum of TiO_2–CuO@GO presented D and G bands at 434.33 and 613.77 cm^{-1}, respectively, with a 2D band centered at 1427.88 cm^{-1} (Fig. 4b). Notably, the D band corresponds to the breathing mode of *k*-point phonons of A_{1g} symmetry and is associated with edge defects and vibrations of C sp^3 atoms. Meanwhile, the G band is associated with the E_{2g} phonon of C sp^2 atoms.[83,84] The intensity ratio between the D and G bands (I_D/I_G) indicates the proportion of structural defects on the sample surface.[85] Despite the similarities between the Raman spectra of both samples, their I_D/I_G ratios differed significantly. In particular, TiO_2–CuO@GO displayed a lower I_D/I_G ratio (0.70) than GO (0.84), indicating that the anchoring/grafting of TiO_2–CuO NPs onto GO nanosheets resulted in fewer structural defects and a more ordered structure, consistent with the XRD findings. The variation in intensity ratios between GO and TiO_2–CuO@GO might be attributed to the enhanced hybridization within the prepared bionanocomposite.

In the FTIR spectrum of GO, distinct absorption bands were observed at wavenumbers of 3423.69, 2976.37, 2344.98, 1631.42, 1385.69, 1052.19, and 661.84 cm^{-1} (Fig. 4c). Among these, the broad band at 3423.69 cm^{-1} corresponded to the hydroxyl (–OH) groups of absorbed water molecules and the stretching of –OH groups chemically bonded to GO. Meanwhile, the narrow absorption band at 2976.37 cm^{-1} was attributed to the symmetric stretching vibration of the C–H group.[86] Furthermore, the bands at 2344.98 and 1631.42 cm^{-1} corresponded to C=C stretching, which occurred as a result of the oxidation of GO. The band at 1385.69 cm^{-1} was associated with O–H bending in phenols, whereas the absorption band at 1052.19 cm^{-1} corresponded to the stretching vibration of the C=O bond.[87] The band corresponding to C–O–C stretching oscillation was observed at 661.84 cm^{-1}, aligning with the findings of Muqoyyanah *et al.*[75] These stretching peaks confirmed the successful oxidation of graphite and the presence of numerous oxygen-containing functional groups in the synthesized GO. The FTIR spectrum of the mycogenic TiO_2–CuO@GO bionanocomposite revealed several absorption bands at 3370.38, 1718.52, 1421.02, 1229.39, 1053.14, 930.91, 688.67, 550.11, and 422.04 cm^{-1} (Fig. 4b). Among these, the intense broad absorption band at 3370.38 cm^{-1} corresponded to –OH stretching vibrations. Meanwhile, the absorption peak at 1718.52 cm^{-1} was characteristic of C=O stretching vibrations in either carboxyl or carbonyl groups.[88] The peak at 1421.02 cm^{-1} was attributed to the bending vibration of unsaturated C=C bonds and CO–H groups.[89] Meanwhile, the peak at 1053 cm^{-1} corresponded to the stretching oscillations of C–O and C–O–C bonds in carboxylic or epoxy groups.[90] The absorption peaks of metal stretching appeared near 500 cm^{-1}. Despite similarities with the FTIR spectrum of GO, the spectrum of TiO_2–CuO@GO displayed notable differences in peak intensities, which was attributed to the grafting and crystalline arrangement of TiO_2 and CuO NPs onto GO laminates. A previous study reported comparable results for a GO hybrid material modified with Ag NPs.[85] The FTIR spectra confirmed the key role of *T. virens* filtrate as a natural bio-reducing, -capping, and -stabilizing agent in the mycosynthesized bionanocomposite.

Next, GO and TiO_2–CuO@GO were analyzed using XPS to determine their elemental compositions as well as the chemical and electronic oxidation states of their species (Fig. 5). The XPS scan survey spectrum of GO displayed peaks characteristic of elemental C 1s and O 1s (Fig. 5a), whereas the full scan survey spectrum of the mycogenic TiO_2–CuO@GO bionanocomposite revealed peaks attributed to Cu 2p, Ti 2p, C 1s, and O 1s (Fig. 5a). The C 1s spectrum of GO was deconvoluted into four subpeaks at binding energies of 284.50, 285.79, 286.50, and 287.95 eV, corresponding to C=C, C–N, C–O, and C=O bonds, respectively (Fig. 5b).[91] Meanwhile, the C 1s spectrum of

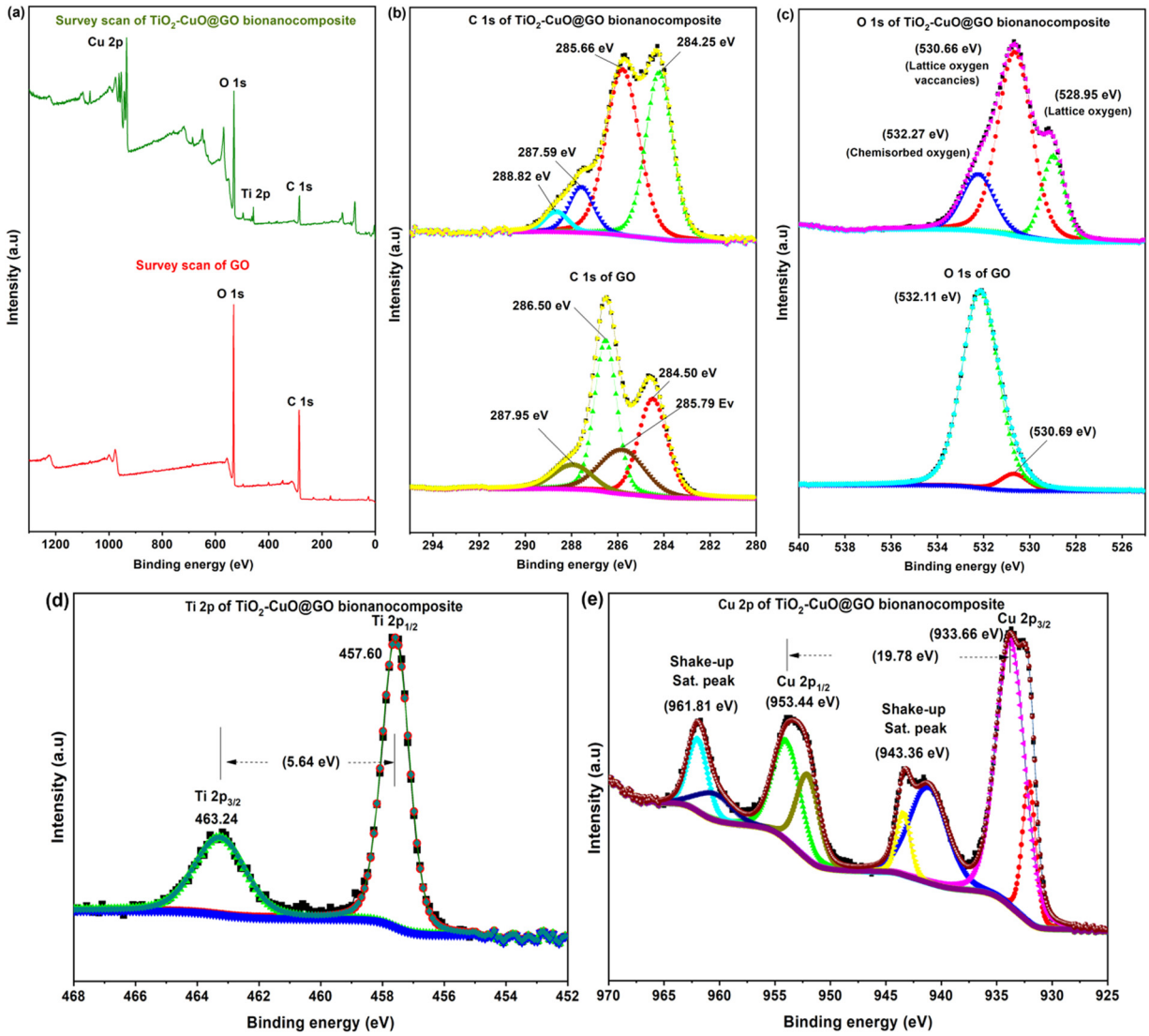

Fig. 5 XPS full scan survey spectra of GO and the mycogenic TiO_2–CuO@GO bionanocomposite (a), C 1s high-resolution spectra of GO and TiO_2–CuO@GO (b), O 1s high-resolution spectra of GO and TiO_2–CuO@GO (c), Ti 2p high-resolution spectrum of TiO_2–CuO@GO (d), and Cu 2p high-resolution spectrum of TiO_2–CuO@GO (e).

TiO_2–CuO@GO exhibited four subpeaks with binding energies of 284.25, 285.66, 287.59, and 288.82 eV (Fig. 5b). In the high-resolution XPS spectrum of the O 1s region of GO, distinct peaks appeared at binding energies of 530.69 and 532.11 eV, corresponding to C═O and O–C═O groups, respectively (Fig. 5c). Meanwhile, the O 1s spectrum of TiO_2–CuO@GO displayed three component peaks at binding energies of 528.95, 530.66, and 532.27 eV, corresponding to lattice oxygen, lattice oxygen vacancies, and chemisorbed oxygen, respectively (Fig. 5c).[92,93] These peaks at binding energies of 528.95, 530.66, and 532.27 eV were further attributed to Ti–OH, C–OH, and –OH termination, respectively, as reported by Bharat and Babu.[94] Shifts to lower and higher binding energies in the C 1s and O 1s spectra were observed after grafting GO onto the mycogenic TiO_2 and CuO NPs, owing to the interactions between the metal oxides and GO carbon network. The high-resolution Cu 2p spectrum of TiO_2–CuO@GO presented two primary peaks at binding energies of 933.66 and 953.44 eV, corresponding to Cu $2p_{3/2}$ and Cu $2p_{1/2}$, respectively, with a spin–orbit splitting of 19.78 eV (Fig. 5d). The Cu $2p_{3/2}$ peak was further deconvoluted into two subpeaks at 932.12 and 933.72 eV, whereas the Cu $2p_{1/2}$ peak was deconvoluted into two subpeaks at 952.10 and 954.10 eV. Two satellite peaks were also identified at binding energies of 943.36 and 961.81 eV. These results confirmed the presence of Cu^{2+} oxidation state, rather than Cu_2O, in the bionanocomposite, consistent with the findings of Ceylan *et al.*[95] and Wang *et al.*[96] Furthermore, the Ti 2p spectrum of the bionanocomposite displayed two high-resolution symmetrical spin–orbit doublet peaks at binding energies of 457.60 and 463.24 eV, corresponding to Ti $2p_{1/2}$ and Ti $2p_{3/2}$, respectively, with a spin–orbit splitting of 5.64 eV (Fig. 5e). The observed binding energies confirmed the presence of Ti^{4+} ions in TiO_2–CuO@GO; however, no evidence for metallic Ti was observed.[97,98] Deconvoluting the Ti $2p_{3/2}$

peak at 457.60 eV revealed the presence of Cu–O–Ti bonds.[94] The prepared bionanocomposite, comprising TiO_2 and CuO NPs, suggests that the observed bonding interactions between the Ti 2p and Cu 2p binding energies in the XPS spectrum are likely mediated through oxygen bridges (Cu–O–Ti). This bonding configuration can be attributed to the presence of oxygen vacancies, which facilitate the formation of such linkages between the two metal oxides. The electronegativity values of Cu and Ti are 1.91 and 1.54, respectively, which boost electron transfer; hence promoting charge transfer *via* electron transfer from Ti^{4+} ions to Cu^{2+} ions.[99,100]

Next, the zeta potentials of GO and TiO_2–CuO@GO were measured in an ethylene glycol matrix under neutral pH conditions to assess their stability. GO exhibited a negative zeta potential value of −36.8 mV with a deviation of 126 mV, which could be attributed to the ionization of carboxylic acid groups and the presence of other negatively charged functionalities. In contrast, the mycogenic TiO_2–CuO@GO bionanocomposite had a zeta potential value of +25.6 mV with a deviation of 150 mV. The conductivities of GO and TiO_2–CuO@GO were 0.00248 and 0.00139 mS cm^{-1}, respectively. Notably, stable colloidal dispersions are typically characterized by zeta potential values more positive or negative exceeding ±30 mV owing to the electrostatic repulsion between particles.[101] This indicated the good stability of the mycogenic TiO_2–CuO@GO bionanocomposite.

A DLS analysis was performed to estimate the average particle size distribution of GO and TiO_2–CuO@GO (Fig. 6a and b). The *Z*-average hydrodynamic diameters of GO and TiO_2–CuO@GO were determined to be 291.1 and 603.2 nm, respectively, with low polydispersity indices of 0.297 and 0.243, indicating good dispersion (Fig. 6a and b). Notably, DLS measures particle size, which includes both the core particle size and the surrounding hydration layer. Further, it often yields larger nanoparticle sizes owing to the tendency of NPs to agglomerate, leading to greater size estimates. This occurs because DLS measures the hydrodynamic sizes of particles, encompassing any aggregates present in the medium. Colloidal suspensions of NMs sometimes exhibit size polydispersity, implying that they contain particles with varying sizes.[102] However, DLS encounters limitations in precisely detecting very small particles or distinguishing between individual NPs and clusters.

EDX analysis is a semi-qualitative technique used to identify various elements in a tested sample and quantify their percentages. The EDX spectrum of GO displayed characteristic emission peaks of C K with weight and atomic percentages of 67.66% and 73.59%, respectively, and of O K with weight and atomic percentages of 32.34% and 26.41%, respectively (Table S2, ESI†). Emission peaks corresponding to C and O occurred at 0.27 and 0.52 keV, respectively (Fig. 6c and d). While, the EDX spectrum of the mycogenic TiO_2–CuO@GO bionanocomposite revealed emission peaks corresponding to the elements Ti, Cu, O, and C (Fig. 6c and d). The mass percentage compositions of Ti 2p, Cu 2p, O 1s, and C 1s were 11.09%, 10.06%, 49.15%, and 29.70%, respectively (Table S2, ESI†). Ti emission signals were observed at 0.45, 4.5, and 4.9 keV, consistent with the findings reported by Al-Harbi *et al.*[103] Meanwhile, Cu emission peaks were apparent at 1, 8, and 9 keV.[104] The distinct emission peak of elemental oxygen at 0.8 keV confirmed the oxide nature of the mycogenic TiO_2–CuO@GO bionanocomposite. An additional peak at 2.3 keV corresponding to sulfur emissions was also observed. Endophytic fungi, such as *Trichoderma* sp., are known to produce sulfur-containing compounds,[105] which explains the presence of sulfur emission peaks in the EDX spectrum. These emission peaks may have originated from the bioactive molecules produced by *T. virens* acting as capping agents.[106] The above EDX findings align with the previous XPS results, confirming the homogenous elemental distribution within the hybrid bionanocomposite and its successful synthesis.

For HRTEM and FESEM analyses, multiple fields were imaged at varying magnifications to ensure comprehensive characterization. HRTEM imaging revealed a nearly transparent, flaky, and

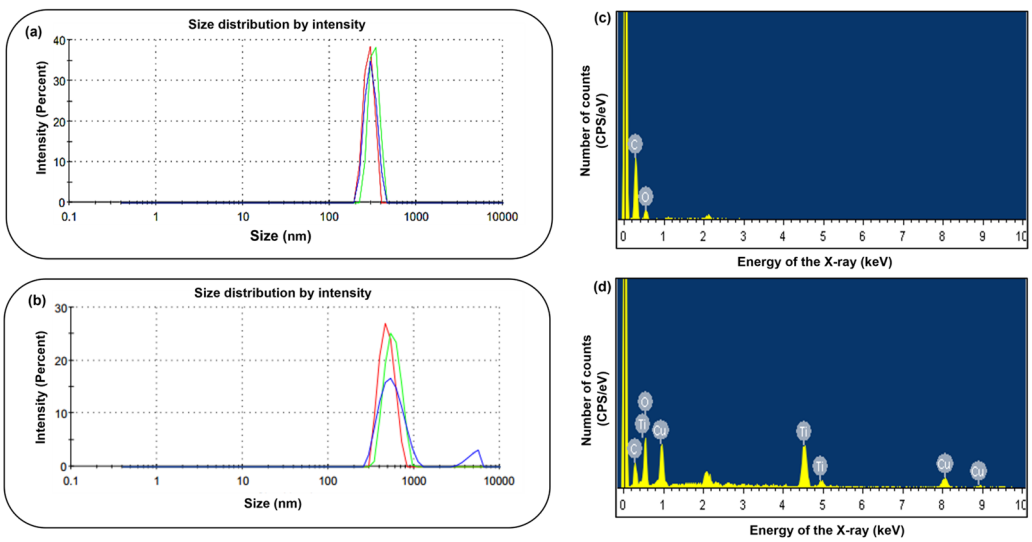

Fig. 6 Average particle size distribution determined by DLS (a) and (b) and FESEM-EDX analysis (c) and (d) for GO and TiO_2–CuO@GO, respectively.

layered ultrastructure with minimal wrinkles for the GO nanosheets (Fig. 7a). Meanwhile, the ultrastructure of the bionanocomposite appeared distinctly different from that of GO, displaying more pronounced folding, which could be attributed to the interaction of TiO_2 and CuO NPs with the GO nanosheets (Fig. 7b–f). The bionanocomposite revealed densely aggregated, opaque, rounded/semi-spherical spots of TiO_2 NPs, along with longitudinal rod-shaped CuO NPs, deposited/loaded onto the GO nanosheets. Similar morphological features have been reported for CuO–GO/TiO_2 nanocatalysts prepared *via* coprecipitation.[107] The lattice fringes of the bionanocomposite are represented in Fig. (7g). The selected area electron diffraction (SAED) pattern of TiO_2–CuO@GO revealed distinct ring structures, confirming the polycrystalline nature of the mycogenic bionanocomposite (Fig. 7h). These SAED ring patterns aligned well with the XRD data, indicating the formation of a highly crystallized nanocomposite. Cross-sectional FE-SEM photomicrographs of GO revealed a smooth, flat, and densely packed structure comprising flaky nanosheets (Fig. 8a). These nanosheets featured wrinkles and folded regions, forming a layered architecture characterized by ultrathin films with multiple folds. These structural features were likely attributed to the presence of sp^3 carbon atoms and oxygen-containing functional groups in the basal planes, contributing to the structural defects in GO.[81] In the mycogenic TiO_2–CuO@GO bionanocomposite, the green-synthesized TiO_2–CuO NPs were grafted onto the GO nanosheets, resulting in an undulating and wrinkled GO surface (Fig. 8b–f). Herein, the TiO_2 NPs exhibited a rounded/quasi-spherical morphology, while the CuO NPs displayed a plate/flake-shaped structure with blade-like edges. The integration of TiO_2 and CuO NPs onto the GO support improved both the uniformity and crystallinity of the synthesized bionanocomposite.

3.3. *In vitro* antibacterial activity of the mycogenic TiO_2–CuO@GO

The antibacterial efficiency of GO and TiO_2–CuO@GO against various foodborne pathogens and bacterial phytopathogens were evaluated using a disc diffusion qualitative assay (Fig. 9). Clear zones of inhibition (ZOIs) were observed surrounding the 8-mm discs and were measured using a digital caliper. The mycogenic TiO_2–CuO@GO bionanocomposite demonstrated notable antibacterial activity against the tested bacterial pathogens. The order of its antibacterial potency was as follows: streptomycin-resistant *Xcc* (17.46 ± 0.19 mm), *E. coli* (15.13 ± 1.47 mm), wild-type streptomycin-susceptible *Xcc* (15.07 ± 0.60 mm), *S. enterica* (12.35 ± 1.23 mm), *Cmc* (11.95 ± 0.95 mm), *Cmm* (11.54 ± 0.39 mm), streptomycin-resistant *Pcc* (10.84 ± 0.11 mm), wild-type streptomycin-susceptible *Pcc* (10.73 ± 0.25 mm), and *S. aureus* (9.69 ± 0.60 mm) (Fig. 9a–i). The disc diffusion assay results indicated that TiO_2–CuO@GO was highly effective against a broad range of foodborne and phytopathogenic bacteria. Notably, the synthesized GO exhibited no antibacterial effects against any of the tested pathogens as shown in Fig. 9. The negative control, ethylene glycol, displayed no antibacterial activity against the tested pathogenic bacterial strains in the disc diffusion assay (Fig. 9). Interestingly, the antibacterial performance, indicated by the ZOI, of the bionanocomposite surpassed that of streptomycin (concentration of 0.1 mg mL^{-1}) against all the tested pathogenic bacteria, except for *Cmm*, *as* illustrated in Fig. 10. In a previous study, GO–CuO was observed to exhibit antibacterial potential against *E. coli* and *S. aureus* with ZOIs of 12.5 ± 2.1 mm and 17.3 ± 2.3 mm, respectively.[108] Furthermore, green-synthesized GO–CuO–ginger essential oil was observed to exhibit antibacterial effects against *E. coli* (15.5 ± 1.3 mm) and *S. aureus* (19.4 ± 0.6 mm) with MICs of 6.25 and 12.5 μg mL^{-1} and MBCs of 25 and 13 μg mL^{-1}, respectively.[109] Meanwhile, GO synthesized from recovered carbon black sourced from waste tires was reported to demonstrate antibacterial activity against *S. aureus*, *E. coli*, *Bacillus subtilis*, and *Pseudomonas aeruginosa* with ZOIs ranging from 6 to 15 mm in a disc diffusion assay.[110] In another study, GO prepared *via* a thermal route was observed to display relatively weak antibacterial effects against *S. aureus*, *E. coli*, *B. subtilis*, *P. aeruginosa*, *B. cereus*, and

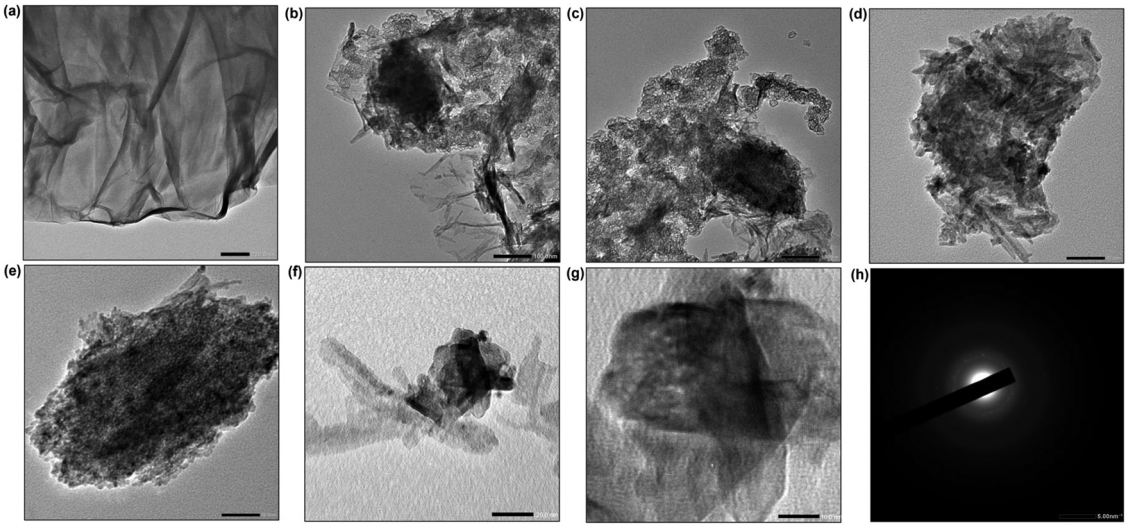

Fig. 7 Morphological characterization using HRTEM showing the ultra-morphological structure of GO (a) and TiO_2–CuO@GO bionanocomposite (b)–(f) at different magnification scales (50 and 100 nm), lattice fringes (g), and SAED pattern of the bionanocomposite (h).

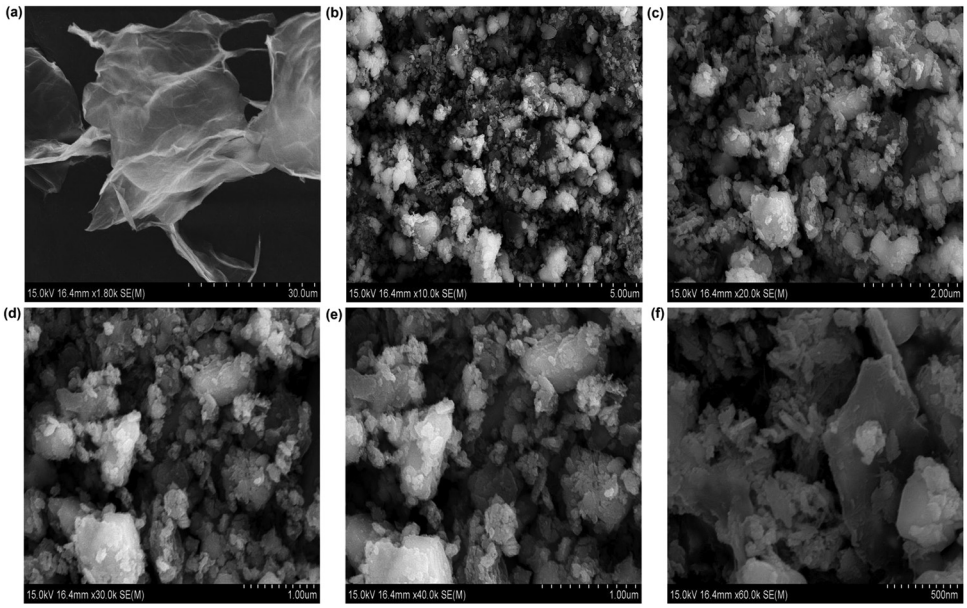

Fig. 8 Structural characterization using FESEM showing the morphological observation of GO (a) and TiO_2–CuO@GO bionanocomposite (b)–(f) at different magnifications.

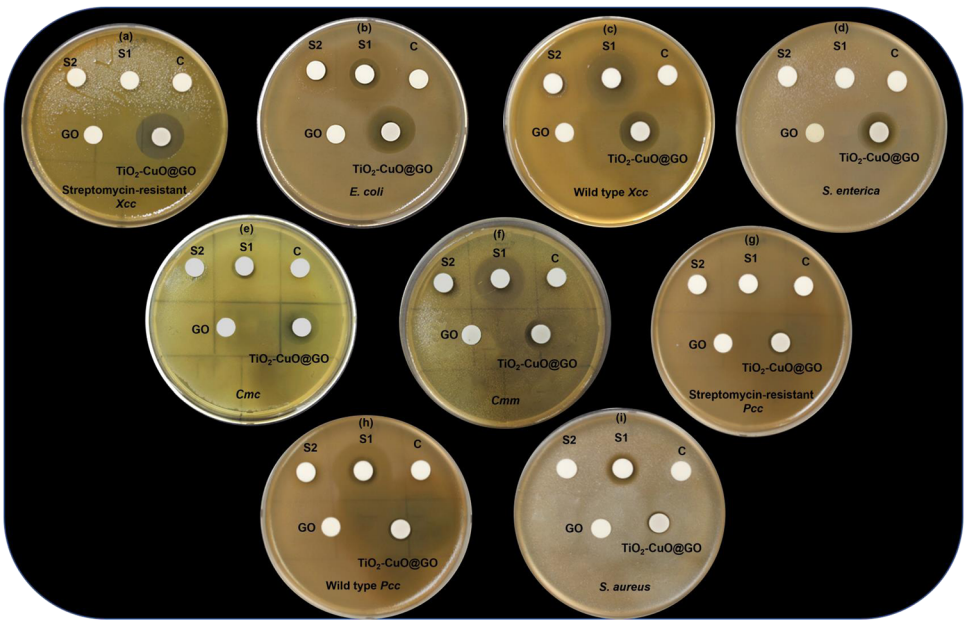

Fig. 9 Photographic images of the plate disc diffusion assay showing the ZOI of TiO_2–CuO@GO bionanocomposite and GO against streptomycin-resistant *Xcc* (a), *E. coli* (b), wild type streptomycin-susceptible *Xcc* (c), *S.* enterica (d), *Cmc* (e), *Cmm* (f), streptomycin-resistant *Pcc* (g), wild type streptomycin-susceptible *Pcc* (h), and *S. aureus* (i). Positive control included streptomycin (S1; 1 mg mL^{-1} and S2; 0.1 mg mL^{-1}) and negative control included ethylene glycol (100%).

Candida albicans.[27] Furthermore, a different study reported that $CoTi_{0.2}Fe_{1.8}O_4$/GO nanocomposites (6 mg mL^{-1} and 1.5 mg mL^{-1}) resulted in ZOIs of 52.3 ± 0.7 mm and 12.4 ± 0.6 mm for *P. aeruginosa* and *S. aureus*, respectively.[111]

This study adopted a quantitative antibacterial approach by determining the MICs and MBCs using a broth microdilution assay to further confirm the antibacterial effectiveness of TiO_2–CuO@GO (Table 1). The MIC is defined as the lowest concentration of an antimicrobial agent that inhibits visible bacterial growth, while the MBC is the lowest concentration that kills bacterial cells. The mycogenic TiO_2–CuO@GO bionanocomposite exhibited MICs of 1.25 mg mL^{-1} against *Cmm*, streptomycin-susceptible wild-type *Xcc*, and streptomycin-resistant *Xcc*; 2.5 mg mL^{-1} against *Cmc*, streptomycin-susceptible wild-type

Pcc, streptomycin-resistant *Pcc*, *E. coli*, and *S. Typhimurium*; and 5 mg mL^{-1} against *S. aureus*. The corresponding MBC values were 2.5 mg mL^{-1} against *Cmm* and streptomycin-susceptible and -resistant *Xcc*; 5 mg mL^{-1} against *Cmc*, streptomycin-susceptible and -resistant *Pcc*, *E. coli*, and *S. enterica*; and 10 mg mL^{-1} against *S. aureus*. The MICs and MBCs of *T. virens*-mediated CuO NPs and TiO_2 NPs against the tested pathogenic bacteria were determined and reported in our previous study.[55] The antibacterial efficacy of TiO_2–CuO@GO against the tested bacterial strains was linked to differences in the bacterial cell walls. For instance, the cell walls of Gram-positive bacteria possess a thick peptidoglycan layer containing teichoic and lipoteichoic acids, forming a robust barrier. However, these bacteria do not feature an outer membrane. In contrast, Gram-negative bacteria possess a thin peptidoglycan layer with an additional outer membrane containing lipopolysaccharides that provide structural integrity. This fundamental difference in the bacterial cell wall structure can substantially influence the ability of antimicrobial agents to penetrate and disrupt bacterial cells.

Interestingly, GO alone did not demonstrate any antibacterial activity. However, when TiO_2 and CuO NPs were grafted onto GO *via* the fungal filtrate, the resulting TiO_2–CuO@GO bionanocomposite exhibited remarkable broad-spectrum antibacterial activity. This is because hybrid nanocomposites of GO and metal NPs demonstrate exceptional antimicrobial properties owing to the synergistic interactions between their individual components, which improved their physicochemical and optical properties. The microbiocidal effectiveness of NMs is influenced by a complex interplay among several critical factors, including size, shape, surface functionalization, charge, chemical composition, and aggregation state.[72] Nanostructures attack bacterial cells through several simultaneous mechanisms. Ti^{4+} and Cu^{2+} ions, released through controlled processes, bind to the carboxylic and amino functionalities on the bacterial surface, disrupting membrane function and cellular respiration.[112,113] Furthermore, oxidative stress caused by the release of reactive oxygen species (ROS) (*e.g.*, superoxide and hydroxyl radicals) induces DNA damage, protein deactivation, and enzymatic activity impairment.[114]

Table 1 MICs and MBCs of the mycogenic TiO_2–CuO@GO against the tested bacterial pathogens

	TiO_2–CuO@GO bionanocomposite	
	MIC (mg mL^{-1})	MBC (mg mL^{-1})
Phytopathogenic bacteria		
Cmm	1.25	2.5
Cmc	2.5	5.0
Streptomycin-susceptible wild type *Pcc*	2.5	5.0
Streptomycin-resistant *Pcc*	2.5	5.0
Streptomycin-susceptible wild type *Xcc*	1.25	2.5
Streptomycin-resistant *Xcc*	1.25	2.5
Foodborne pathogenic bacteria		
E. coli	2.5	5.0
S. enterica	2.5	5.0
S. aureus	5.0	10.0

The noteworthy antibacterial efficacy of TiO_2–CuO@GO could be attributed to several multifaceted mechanisms (Fig. 11), including the following: (i) mechanical disruption or the ''knife effect,'' where the sharp edges of GO pierce bacterial cells and disintegrate their internal structures, demonstrating biocidal action; (ii) oxidative stress and ROS generation, particularly superoxide anions, which disrupt cellular components such as proteins, DNA, and lipids, inducing cell dysfunction and subsequent cellular death; (iii) interactions of GO's functional groups with bacterial cell membranes; and (iv) synergistic effects owing to the surface decoration/grafting of the GO surface with metal oxide-based NPs.[115,116] The enveloping or wrapping of bacterial cells by GO nanoflakes disrupts their interactions with the surrounding growth environment, impeding cellular viability and ultimately causing cell death.[117] Once

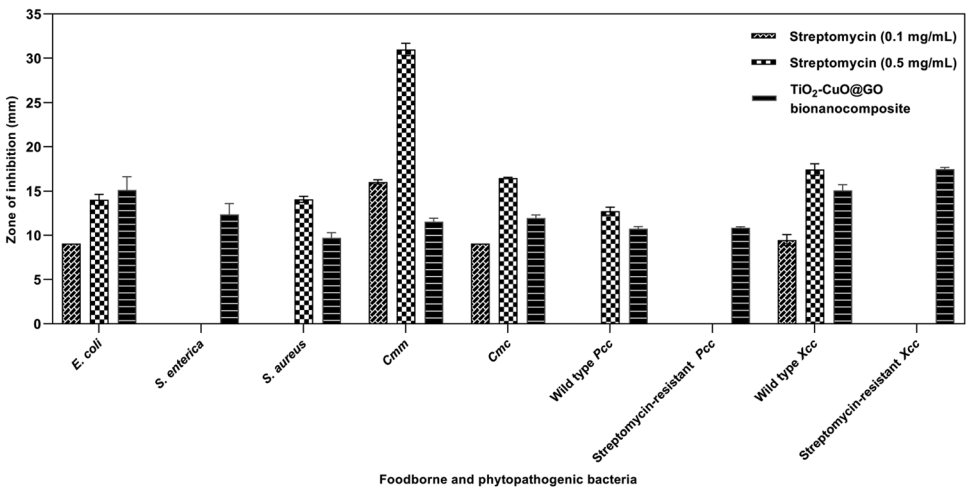

Fig. 10 Graphical representation of the antibacterial disc diffusion assay of TiO_2–CuO@GO bionanocomposite against streptomycin-resistant *Xcc*, *E. coli*, wild type *Xcc*, *S.* enterica, *Cmc*, *Cmm*, streptomycin-resistant *Pcc*, wild type *Pcc*, and *S. aureus*. The data shown represent the averages ± SD of three independent replicates. ZOI of streptomycin against the tested pathogens was highlighted as a key metric for comparative analysis.[34] The results were statistically significant at $p < 0.0001$.

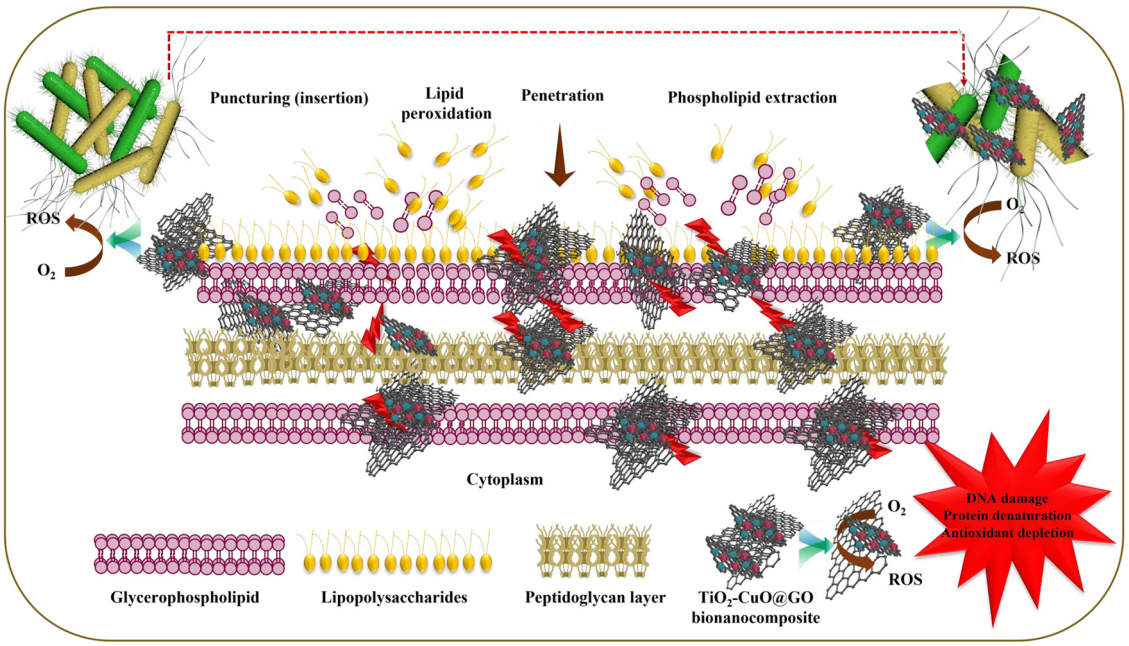

Fig. 11 Proposed antibacterial mechanism of the mycogenic TiO_2–CuO@GO bionanocomposite against the tested bacterial pathogens.

GO sheets adhere to bacterial cells, they wrap around them, establishing a physical barrier. This wrapping effect is facilitated by the flexible, flake-like structure of GO, which allows it to conform to the shape of bacterial cells. Consequently, bacterial cells are isolated from their surrounding environment, hindering nutrient uptake, waste exchange, and cell-to-cell communication, which are crucial for their growth and survival. This results in diminished cellular functions, preventing bacterial reproduction and leading to cell lysis. Eventually, this process notably reduces the bacterial population, enhancing the overall antimicrobial effect.

Furthermore, the antibacterial activity of TiO_2–CuO@GO might be attributed to the physical and/or mechanical disruption caused by structural defects at the edges of GO nanosheets, as revealed by Raman analysis. This physical/mechanical damage occurs *via* two modes of action: insertion and penetration. These modes allow GO to spontaneously pierce bacterial cell membranes, inflicting membrane damage with its sharp edges. The abundant oxygen-based functional groups endow GO with hydrophilicity and high surface energy.[118] The amphiphilic nature of GO, which is ascribed to its hydrophilic edges and hydrophobic planes, enables its interaction with bacterial membranes. Notably, GO nanosheets extract membrane phospholipids through hydrophobic interactions between the lipid bilayer and sp^2 carbons present in the GO nanosheets, disrupting membrane functionality and ultimately leading to bacterial cell disintegration.[119] The interactions of the hybrid bionanocomposite with bacterial cells compromise cell membrane integrity, resulting in its damage.[120] These interactions involve membrane piercing, surface adhesion, wrapping, and lipid peroxidation.[117] ROS generation initiates lipid peroxidation, oxidizing lipid molecules to form lipid peroxide radicals. This process leads to oxidative damage to the bacterial cell membrane, creating lesions that result in the leakage of cellular components.[121] The distinctive two-dimensional nanostructure, sharp edges, and corner protrusions of GO facilitate its penetration into the bacterial cell membrane, thus lowering the energy barrier for membrane disruption. This disruption causes changes in the transmembrane potential and leakage of intracellular constituents and electrolytes. Notably, the oxygen-containing functional groups, such as hydroxyl (–OH), epoxy (C–O–C), carbonyl (–C═O), and carboxyl groups, of GO play a pivotal role in its robust antimicrobial activity through π–π stacking interactions; van der Waals forces; and electrostatic, covalent, and hydrogen bonding.[122] Furthermore, the hydrophobic properties of GO disrupt the lipid bilayers of bacterial membranes, causing destabilization and rupture, leading to the loss of bacterial viability. Moreover, the high electrical conductivity of GO initiates electrochemical cascade reactions that adversely impact bacterial cell surfaces. The electron flow from bacterial cells to oxygenated functional groups on GO disrupts the transmembrane potential, causing membrane depolarization, ion imbalance, loss of membrane integrity, and ultimately cell death.[123] As pointed out, the proposed antibacterial mechanisms are speculative in the absence of direct experimental validation. Hence, future studies will include follow-up experiments to validate the proposed mechanisms and provide a more conclusive understanding of the antibacterial mechanism. Such experiments will focus on quantifying ROS using fluorescent probes,[124] assessing bacterial membrane integrity *via* propidium iodide staining assay,[125] visualizing morphological changes *via* electron microscopy,[7] quantifying lipid peroxidation products,[126] and analyzing expression of genes associated with oxidative stress response to provide more conclusive evidence.[127] By addressing these follow up experiments, the antibacterial mechanism of the bionanocomposite can be further validated.

3.4. Catalytic degradation activity of the mycogenic TiO_2–CuO@GO

The chemical and textile industries are major sources of hazardous organic contaminants, which are among the leading causes of water pollution, posing serious environmental risks.[128] In this study, the catalytic degradation activity of the mycogenic TiO_2–CuO@GO bionanocomposite was tested against CR dye. The effect of contact duration on CR degradation is illustrated in Fig. 12a. As depicted, 70% degradation was achieved within the first 4 min, reaching equilibrium. The degradation performance of TiO_2–CuO@GO was superior to that of CuO NP catalysts reported previously, which can photodegrade 25 mg L^{-1} CR within 120 min.[129] Furthermore, recent studies have used graphene–CuO heterostructures for the photocatalytic degradation of CR over a 180-min period, followed by an additional 180-min period of shaking with CR to enhance dye removal, ultimately achieving a total removal rate of 75%.[130] This reveals the remarkable catalytic degradation activity of the mycogenic TiO_2–CuO@GO nanocatalyst synthesized in this study, minimizing the time required for catalytic CR degradation. By fitting the kinetic profile depicted in Fig. S1 (ESI†) against a pseudo-first-order kinetic model, an R^2 value of 0.9301 was obtained, implying that the catalytic reaction followed pseudo-first–order behavior. Notably, the slope of this linear regression curve corresponds to the rate constant, which was calculated as 0.0268 min^{-1}.[131] This rate constant exceeds that reported by a previous study, which examined the PMS activation of a GO/CuO nanocomposite for the degradation of malachite green and obtained a rate constant of 0.0201 min^{-1}.

An investigation into the effect of the initial concentration of TiO_2–CuO@GO on CR removal revealed that after incubation for 28 min, the removal percentage stabilized across all tested concentrations, with an average value of approximately 68.9% (Fig. 12b). This stability may be attributed to the presence of abundant active sites on the surface of the mycogenic nanocomposite, which facilitated efficient catalytic degradation over the entire range of concentrations.[132] This behavior is similar to that of a ceramic membrane, which was loaded with CuO after PMS activation for CR removal, wherein the removal efficiency decreased from 94.5% to 92.2% (exhibiting a drop of 2.3%) over the concentration range of 20–50 mg L^{-1}.[133] The impact of NaCl concentration on CR degradation was also examined. The results revealed that the presence of NaCl enhanced CR removal from approximately 65% to 91% at NaCl concentrations of 1.5% and 3%, respectively (Fig. 12c). This effect is similar to the influence of NaCl on the $NaBO_2$/PMS system, wherein the salt enhanced the catalytic degradation of the acid red 1 dye.[134] However, the abovementioned effect

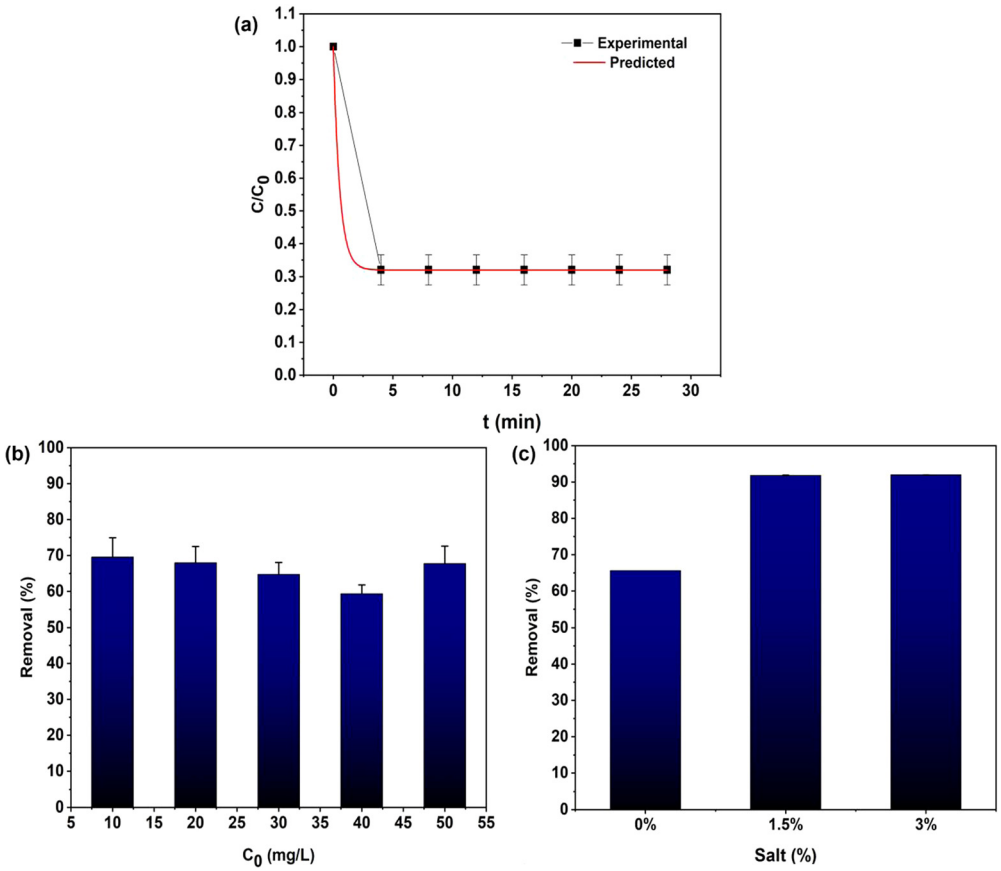

Fig. 12 The effect of contact time on the catalytic degradation of CR using 0.1 g L^{-1} catalyst, 0.8 g L^{-1} PMS, and 20 mg L^{-1} CR (a), the effect of initial concentration of CR on the degradation efficiency using 0.1 g L^{-1} of the catalyst and 0.8 g L^{-1} of PMS (b), and the effect of salt concentration on the degradation efficiency of 20 ppm CR using 0.1 g L^{-1} of catalyst and 0.8 g L^{-1} of PMS (c).

contradicts the influence of NaCl on Fe_3O_4–$CoCO_3$/rGO PMS catalyst activation for Rhodamine-B degradation. In this degradation process, interactions between Cl^- and $SO_4^{-\bullet}$ lead to the formation of less reactive $Cl^\bullet$ and $Cl_2^{-\bullet}$ radicals, which exhibit lower redox potential than $SO_4^{-\bullet}$ radicals, resulting in inferior Rhodamine-B degradation.[135] Optimization of factors such as pH and temperature can significantly influence the efficiency of the degradation process, and their optimization is crucial for a comprehensive understanding of the catalytic performance. These factors highlight areas for future studies. To address these limitations, future research will focus on the implementation of a systematic optimization study to determine the optimum pH and temperature to attain maximum degradation efficiency.

The initial step in CR degradation involves its adsorption onto the catalytic bionanocomposite, whose surface is activated by PMS, leading to the production of $SO_4^{-\bullet}$ and $^\bullet OH$ radical species. Among these species, $SO_4^{-\bullet}$ plays a key role in generating $^\bullet OH$ radicals from OH^- or H_2O (eqn (4)–(8)).[136,137]

$$M^{n+} + HSO_5^- \rightarrow M^{n+1} + SO_5^{-\bullet} + OH^\bullet \quad (4)$$

$$M^{n+} + HSO_5^- \rightarrow M^{n+1} + SO_4^{-\bullet} + OH^- \quad (5)$$

$$SO_4^{-\bullet} + H_2O \rightarrow OH^\bullet + SO_4^{2-} + H^+ \quad (6)$$

$$SO_4^{-\bullet} + OH^- \rightarrow OH^\bullet + SO_4^{2-} \quad (7)$$

$$SO_4^{-\bullet} + OH^\bullet + Dye \rightarrow H_2O + CO_2 \quad (8)$$

Notably, PMS features an asymmetrical structure that facilitates the cleavage of its peroxide bond *via* electron transfer, producing $SO_4^{-\bullet}$ radicals. PMS can be activated through various methods, including heat, ultrasound, UV light exposure, or catalysis. Among these, catalysis is considered the most effective method owing to its simplicity, safety, and low energy and equipment requirements.[138] During catalysis, transition metals with higher transition oxidation states can generate $SO_5^{-\bullet}$ radicals, whereas those with bivalent states decompose PMS to $SO_4^{-\bullet}$ radicals.[139] A previous study reported that bimetallic oxide nanocatalysts exhibit a synergistic mechanism, which enables them to enhance the reaction efficiency compared with monometallic oxide catalysts by forming hydroxyl complexes with the catalyst to generate $SO_4^{-\bullet}$ radicals.[140] The synthesized radicals attack CR, disintegrating it into small molecules, which are subsequently mineralized into carbon dioxide (CO_2) and water (H_2O) (Fig. 13). Furthermore, GO plays a role in increasing the surface area and providing structural support to prevent metal agglomeration. Moreover, it facilitates electron transfer from the targeted contaminants to persulfate, thereby enhancing the catalytic performance of the bionanocomposite. It also promotes the formation of $SO_4^{-\bullet}$ radicals from activated PMS through oxygen-containing functional groups present on its surface. Given the critical importance of long-term stability and reusability for sustainable and economically viable catalytic processes, further studies to assess the stability and recyclability of the bionanocomposite without significant loss of activity are essential to validate its practicality for real-world applications. Future research will focus on evaluating the bionanocomposite's stability under operational conditions, testing its reusability through multiple cycles, and exploring regeneration techniques to sustain its catalytic performance over time while minimizing environmental risks. By addressing these factors, the TiO_2–CuO@GO bionanocomposite can be established as a sustainable and cost-effective material for environmental applications. Moreover, in this study, the focus was on evaluating the efficiency of CR removal by the TiO_2–CuO@GO. While the results demonstrate effective degradation, the analysis of intermediates was not conducted. The lack of analysis of degradation intermediates represents a limitation of the current study; however, future work will focus on identifying and characterizing these byproducts, assessing their toxicity, and optimizing the process to achieve complete mineralization. By addressing these aspects, the environmental safety and practical applicability of the bionanocomposite can be further implemented.

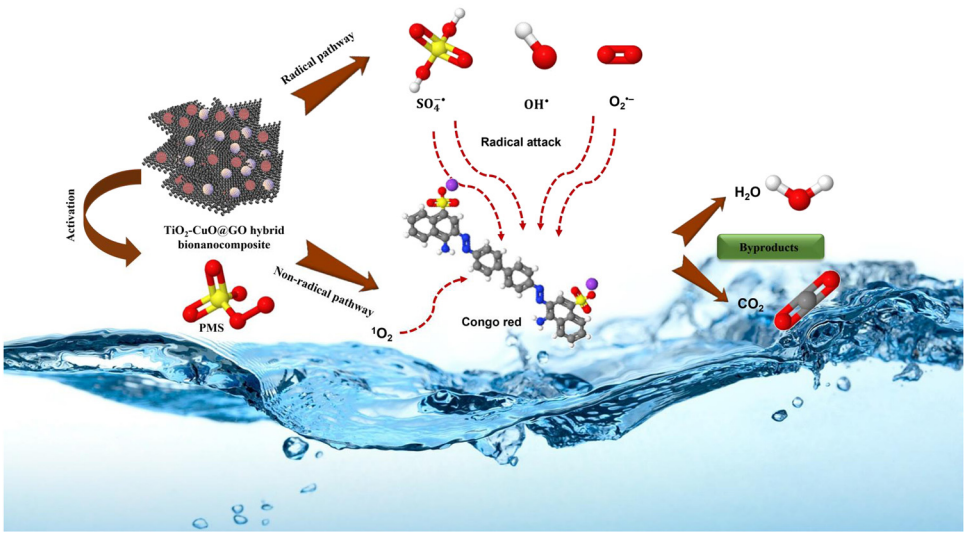

Fig. 13 Schematic diagram representing the catalytic degradation of CR *via* PMS-assisted catalytic activation by TiO_2–CuO@GO bionanocomposite.

4. Conclusions

Nanocomposites are gaining increasing attention as advanced, multifunctional nanoformulations owing to their ability to synergistically combine the unique properties of their individual components. This study involved the synthesis of GO nanosheets using a modified Tour's method and subsequently grafted them onto mycosynthesized TiO_2 and CuO NPs using *T. virens*. The structural, optical, vibrational, and morphological properties of GO and the synthesized TiO_2–CuO@GO bionanocomposite were analyzed. UV/Vis spectral analysis revealed an absorption band characteristic of GO near approximately 230 nm, whereas TiO_2–CuO@GO displayed absorption bands at wavelengths of approximately 232, 361, and 422 nm, corresponding to GO, CuO, and TiO_2, respectively. Furthermore, the optical band gap energies of GO and TiO_2–CuO@GO were 2.68 and 2.76 eV, respectively. XRD data revealed average crystallite sizes of 10.65 and 25.41 nm for GO and TiO_2–CuO@GO, respectively. Moreover, HRTEM and FE-SEM indicated that that GO exhibited a nearly transparent, flaky, layered structure with minimal folds and wrinkles, whereas TiO_2–CuO@GO displayed an undulated, wrinkled surface decorated with rounded/quasi-spherical TiO_2 NPs and plate/flake-shaped CuO NPs. The bionanocomposite was free of impurities or other secondary phases.

The mycogenic TiO_2–CuO@GO bionanocomposite exhibited broad-spectrum antibacterial activity against various foodborne and plant pathogenic bacteria. The Kirby–Baur assay revealed that TiO_2–CuO@GO showed maximum and minimum growth inhibition against the Gram-negative streptomycin-resistant strain *Xcc* (17.46 ± 0.19 mm) and Gram-positive *S. aureus* (9.69 ± 0.60 mm) at a concentration of 20 mg mL^{-1}, respectively. The superior antibacterial activity of the synthesized bionanocomposite may be attributed to its small size and unique nano configuration. Furthermore, this antibacterial effect likely involved multiple antibacterial mechanisms as follows: (i) release of Ti^{4+} and Cu^{2} ions, production of ROS, and initiation of oxidative stress cascades; (ii) physical and/or mechanical disruption caused by structural defects at the edges of GO nanosheets; and (iii) enveloping/wrapping of bacterial cells by GO nanoflakes, impeding their interactions with the surrounding growth environment. Additionally, TiO_2–CuO@GO at initial concentrations of 10–50 mg L^{-1} achieved PMS-activated degradation of CR dye within 28 min, showing an efficiency of 70%. Thus, our findings highlight the significant potential of the mycogenic TiO_2–CuO@GO bionanocomposite as an effective antimicrobial agent for controlling foodborne and phyto bacterial pathogens as well as a nanocatalyst for purifying wastewater contaminated with dyes.

Scaling up the TiO_2–CuO@GO bionanocomposite for real-world applications will necessitate optimizing the mycosynthesis process, incorporating the material into functional systems, and conducting pilot-scale testing. Automated bioreactors could be employed to boost the efficiency and scalability of the fungal cultivation and the synthesis process. The nanocomposite can be incorporated into filters and membranes for specific applications, such as wastewater treatment or as coatings for antimicrobial surfaces. Pilot-scale studies should be conducted under real-world conditions, such as varying pollutant concentrations, flow rates, and environmental factors. However, challenges such as ensuring the long-term stability and reusability of the bionanocomposite require thorough investigation. Additionally, addressing production costs, securing regulatory approval, and gaining public acceptance are critical steps toward commercialization. By overcoming these barriers, the TiO_2–CuO@GO bionanocomposite has the potential to significantly contribute to solving global challenges in pollution mitigation, healthcare, and sustainable agriculture.

Author contributions

Basma A. Omran: literature search, data acquisition, investigation, visualization, validation, data analysis, data curation and interpretation, microscopic analysis, writing, review, and editing; M. O. Abdel-Salam: GO preparation, investigation, data curation; Hebatullah H. Farghal: investigation and visualization; Mayyada M. H. El-Sayed: review and editing; Kwang-Hyun Baek: funding acquisition, review, and editing.

Data availability

The authors declare that the data supporting the findings of this study are available within this document.

Conflicts of interest

The authors declare that they have no conflict of interest.

Acknowledgements

This research was carried out with the support of the Cooperative Research Program for Agriculture Science and Technology Development, RDA, Republic of Korea, and the American University in Cairo. Authors would like to thank Dr Muhammad Fazle Rabbee for his assistance during the work.

References

1 X. Yin, J. Shan, L. Dou, Y. Cheng, S. Liu, R. Y. A. Hassan, Y. Wang, J. Wang and D. Zhang, Multiple bacteria recognition mechanisms and their applications, *Coord. Chem. Rev.*, 2024, **517**, 216025.
2 M. Lutfi, M. Ashraf and N. Ullah, A critical review on the removal of anionic dyes by cross-linked resin: Recent progress, challenges and future perspective, *Sep. Purif. Technol.*, 2025, **360**, 131111.
3 R. R. Wittler, Foodborne and waterborne illness, *Pediatr. Rev.*, 2023, **44**, 81–91.
4 J. Wang, X. Cui, L. Liang, J. Li, B. Pang and J. Li, Advances in DNA-based electrochemical biosensors for the detection of foodborne pathogenic bacteria, *Talanta*, 2024, **275**, 126072.
5 S. Bhatt, R. Pathak, V. D. Punetha and M. Punetha, Chitosan nanocomposites as a nano-bio tool in phytopathogen control, *Carbohydr. Polym.*, 2024, **331**, 121858.

6 L.-L. He, L.-T. Xiong, X. Wang, Y.-Z. Li, J.-B. Li, Y. Shi, X. Deng and Z.-N. Cui, Application of inhibitors targeting the type III secretion system in phytopathogenic bacteria, *Chinese Chem. Lett.*, 2024, **36**, 110044.
7 B. A. Omran, M. Fazle and K. Baek, Biologically inspired nanoformulations for the control of bacterial canker pathogens *Clavibacter michiganensis* subsp. *michiganensis* and subsp. *capsici*, *J. Biotechnol.*, 2024, **392**, 34–47.
8 N. V. Fotina, Y. R. Serazetdinova, D. E. Kolpakova, L. K. Asyakina, V. V. Atuchin, K. M. Alotaibi, G. Mudgal and A. Y. Prosekov, Enhancement of wheat growth by plant growth-stimulating bacteria during phytopathogenic inhibition, *Biocatal. Agric. Biotechnol.*, 2024, **60**, 103294.
9 Y. Shi, Z.-S. Zhang, J. Shao, C. Fu, L.-T. Xiong, Z.-D. Li and Z.-N. Cui, Photoinduced palladium-catalyzed 1, 3-diene-selective fluoroalkylamination compounds as potential bactericidal agent against *Xanthomonas oryzae* pv. *oryzae*, *Chinese Chem. Lett.*, 2024, **35**, 108794.
10 Q. Le Dang, H. T. T. Do, G. J. Choi, M. Van Nguyen, H. D. Vu, G. V. Pham, C. T. Ho, X. C. Nguyen, T. D. Tran and D. T. Nghiem, *In vitro* and *in vivo* antimicrobial activities of extracts and constituents derived from *Desmodium styracifolium* (Osb.) Merr. against various phytopathogenic fungi and bacteria, *Ind. Crops Prod.*, 2022, **188**, 115521.
11 M. Shahid and M. S. Khan, Ecotoxicological implications of residual pesticides to beneficial soil bacteria: A review, *Pestic. Biochem. Physiol.*, 2022, **188**, 105272.
12 B. A. Omran and K.-H. Baek, Control of phytopathogens using sustainable biogenic nanomaterials: Recent perspectives, ecological safety, and challenging gaps, *J. Cleaner Prod.*, 2022, **372**, 133729.
13 R. S. Riseh, M. Vatankhah, M. Hassanisaadi and J. F. Kennedy, Chitosan/silica: A hybrid formulation to mitigate phytopathogens, *Int. J. Biol. Macromol.*, 2023, **239**, 124192.
14 B. Peng, J. Qin, Y. Li, K. Wu, Y. Kuang and F. Jiang, Recent advances in nanomaterials-enabled active food packaging: nanomaterials synthesis, applications and future prospects, *Food Control*, 2024, **163**, 110542.
15 P. O. Oladoye, M. O. Bamigboye, O. D. Ogunbiyi and M. T. Akano, Toxicity and decontamination strategies of Congo red dye, *Sustainable Dev.*, 2022, **19**, 100844.
16 V. Reyes-Márquez, L. E. C. Rojas, R. Colorado-Peralta, R. Peña-Rodríguez, J. M. Rivera-Villanueva and D. Morales-Morales, Adsorption potential of polymeric porous crystalline materials (MOFs) for the removal of Indigo carmine, Congo red, and Malachite green from water, *Inorganica Chim. Acta*, 2023, **558**, 121743.
17 E. Brillas and R. Oliver, Development of persulfate-based advanced oxidation processes to remove synthetic azo dyes from aqueous matrices, *Chemosphere*, 2024, **355**, 141766.
18 K. Naseem, Z. H. Farooqi, R. Begum and A. Irfan, Removal of Congo red dye from aqueous medium by its catalytic reduction using sodium borohydride in the presence of various inorganic nano-catalysts: A review, *J. Cleaner Prod.*, 2018, **187**, 296–307.
19 D. Marghade, S. Shelare, C. Prakash, M. E. M. Soudagar, T. M. Y. Khan and M. A. Kalam, Innovations in metal-organic frameworks (MOFs): Pioneering Adsorption approaches for persistent organic pollutant (POP) Removal, *Environ. Res.*, 2024, **258**, 119404.
20 M. H. M. Noor and N. Ngadi, Global research landscape on coagulation-flocculation for wastewater treatment: A 2000–2023 bibliometric analysis, *J. Water Process Eng.*, 2024, **64**, 105696.
21 J. Gao, X. Xing, W. Cai, Z. Li, G. Shi, Y. Chen, H. Liang, C. Chen, K. Ma and J. Chen, Effect of micropollutants on disinfection byproducts and antibiotic resistance genes in drinking water in the process of biological activated carbon treatment, *J. Hazard. Mater.*, 2024, **461**, 132304.
22 S. Bandehali, A. Moghadassi, S. M. Hosseini, F. Parvizian, D. Ghanbari, R. Rahimizadeh and A. A. Ebrahimi, Smart ion exchange membrane with high impact in heavy metals separation prepared by electrospinning process with ultrasensitive responsiveness for water treatment, *Chem. Eng. Res. Des.*, 2024, **205**, 763–774.
23 L. Hejji, Y. A. E. H. Ali, A. Azzouz, N. Raza, L. P. Villarejo and S. K. Kailasa, Recent insights into molecularly imprinted membrane technology for removal of pollutants from environmental water: From organic molecules to metal ions, *J. Water Process Eng.*, 2024, **58**, 104852.
24 Z. U. Zango, K. S. Khoo, A. Garba, Z. N. Garba, U. N. Danmallam, O. Aldaghri, K. H. Ibnaouf, N. M. Ahmad, A. M. Binzowaimil and J. W. Lim, A review on titanium oxide nanoparticles modified metal-organic frameworks for effective CO_2 conversion and efficient wastewater remediation, *Environ. Res.*, 2024, **252**, 119024.
25 M. Kurian, Advanced oxidation processes and nanomaterials -a review, *Clean. Eng. Technol.*, 2021, **2**, 100090.
26 M. O. Abdel-Salam and T. Yoon, Cobalt-ferrite/Ag-fMWCNT hybrid nanocomposite catalyst for efficient degradation of synthetic organic dyes via peroxymonosulfate activation, *Environ. Res.*, 2022, **205**, 112424.
27 K. Bentedlaouti, A. Belouatek and N. Kebaili, Antibacterial and antioxidant activities of graphene and graphene oxide synthesis coated silver nanoparticules, *J. Cryst. Growth*, 2024, **627**, 127527.
28 N. D. Hai, N. M. Dat, N. T. H. Nam, H. An, L. T. Tai, L. M. Huong, C. Q. Cong, N. T. H. Giang, N. T. Tinh and N. H. Hieu, A review on the chemical and biological synthesis of silver nanoparticles@graphene oxide nanocomposites: A comparison, *Mater. Today Sustain.*, 2023, **24**, 100544.
29 S. P. Kumar, P. C. Sharafudeen and P. Elumalai, High entropy metal oxide@ graphene oxide composite as electrocatalyst for green hydrogen generation using anion exchange membrane seawater electrolyzer, *Int. J. Hydrogen Energy*, 2023, **48**, 38156–38171.
30 M. D. Najafi, A. Ehsani, M. Nabatian, Z. Hamza and N. Neekzad, Advanced supercapacitor electrodes: Synthesis and electrochemical characterization of graphene oxide-bismuth metal-organic framework composites for superior performance, *Electrochim. Acta*, 2024, **498**, 144636.
31 I. Altin, CuO-TiO_2/graphene ternary nanocomposite for highly efficient visible-light-driven photocatalytic degradation of bisphenol A, *J. Mol. Struct.*, 2022, **1252**, 132199.

32 A. B. Migdadi, Q. M. Al-Bataineh, A. A. Ahmad, H. M. Al-Khateeb and A. Telfah, Titanium dioxide/reduced graphene oxide nanocomposites as effective photocatalytic for hazardous 4-nitrophenol, *J. Alloys Compd.*, 2024, **971**, 172794.
33 A. Ahmad, M. Khan, S. M. Osman, A. M. Haassan, M. H. Javed, A. Ahmad, A. Rauf and R. Luque, Benign-by-design plant extract-mediated preparation of copper oxide nanoparticles for environmentally related applications, *Environ. Res.*, 2024, **247**, 118048.
34 B. A. Omran, M. F. Rabbee, M. O. Abdel-Salam and K. H. Baek, Mycofabrication of bimetal oxide nanoparticles (CuO/TiO_2) using the endophytic fungus *Trichoderma virens*: Material properties and microbiocidal effects against bacterial pathogens, *Colloids Surf., A*, 2024, **682**, 132890.
35 A. Islam, I. Rahat, C. Rejeeth, D. Sharma and A. Sharma, Recent advcances on plant-based bioengineered nanoparticles using secondary metabolites and their potential in lung cancer management, *J. Future Foods*, 2025, **5**, 1–20.
36 B. A. Omran, O. Aboelazayem, H. N. Nassar, R. A. El-Salamony and N. S. El-Gendy, Biovalorization of mandarin waste peels into silver nanoparticles and activated carbon, *Int. J. Environ. Sci. Technol.*, 2021, **18**, 1119–1134.
37 T. A. Saleh and G. Fadillah, Green synthesis protocols, toxicity, and recent progress in nanomaterial-based for environmental chemical sensors applications, *Trends Environ. Anal. Chem.*, 2023, **39**, e00204.
38 A. A. Arteaga-Castrejón, V. Agarwal and S. Khandual, Microalgae as a potential natural source for the green synthesis of nanoparticles, *Chem. Commun.*, 2024, **60**, 3874–3890.
39 A. Rana, K. Yadav and S. Jagadevan, A comprehensive review on green synthesis of nature-inspired metal nanoparticles: Mechanism, application and toxicity, *J. Cleaner Prod.*, 2020, **272**, 122880.
40 R. Rahman, T. Chen, Q. Yao, S. Zang and J. Xie, Toward greener synthesis of gold nanomaterials: From biological to biomimetic synthesis, *Coord. Chem. Rev.*, 2021, **426**, 213540.
41 Z. Khanam, S. Gupta and A. Verma, Endophytic fungi-based biosensors for environmental contaminants-A perspective, *S. Afr. J. Bot.*, 2020, **134**, 401–406.
42 P. Mathur, S. Saini, E. Paul, C. Sharma and P. Mehtani, Endophytic fungi mediated synthesis of iron nanoparticles: Characterization and application in methylene blue decolorization, *Curr. Res. Green Sustainable Chem.*, 2021, **4**, 100053.
43 S. Iranmanesh, G. H. Shahidi Bonjar and A. Baghizadeh, Study of the biosynthesis of gold nanoparticles by using several saprophytic fungi, *SN Appl. Sci.*, 2020, **2**, 1851.
44 X. Huang, L. Shi, Y. Lin, C. Zhang, P. Liu, R. Zhang, Q. Chen, X. Ouyang, Y. Gao and Y. Wang, *Pycnoporus sanguineus* polysaccharides as reducing agents: Self-assembled composite nanoparticles for integrative diabetic wound therapy, *Int. J. Nanomed.*, 2023, **18**, 6021–6035.
45 J. Saxena and K. M. Ayushi, Evaluation of *Sclerotinia sclerotiorum* MTCC 8785 as a biological agent for the synthesis of silver nanoparticles and assessment of their antifungal potential against *Trichoderma harzianum* MTCC 801, *Environ. Res.*, 2023, **216**, 114752.
46 N. Moradi, M. Sadravi, S. Hajati and H. Hamzehzarghani, Biosynthesized silver nanoparticles using *Trichoderma harzianum* reduce charcoal rot disease in bean, *Rhizosphere*, 2024, **29**, 100828.
47 A. Raza, S. N. Islam, K. Sayeed, K. Pandey, F. Mashkoor, C. Jeong, M. Shoeb and A. Ahmad, *Fusarium oxysporum* mediated synthesis of nitrogen-doped carbon supported platinum nanoparticles for supercapacitor device and dielectric applications, *J. Ind. Eng. Chem.*, 2025, **141**, 568–581.
48 G. M. Herrera Pérez, L. E. Castellano and C. A. Ramírez Valdespino, *Trichoderma* and mycosynthesis of metal nanoparticles: role of their secondary metabolites, *J. Fungi*, 2024, **10**, 443.
49 B. A. Omran, H. N. Nassar, N. A. Fatthallah, A. Hamdy, E. H. El-Shatoury and N. S. El-Gendy, Characterization and antimicrobial activity of silver nanoparticles mycosynthesized by *Aspergillus brasiliensis*, *J. Appl. Microbiol.*, 2018, **125**, 370–382.
50 B. A. Omran, H. N. Nassar, S. A. Younis, N. A. Fatthallah, A. Hamdy, E. H. El-Shatoury and N. S. El-Gendy, Physiochemical properties of *Trichoderma longibrachiatum* DSMZ 16517-synthesized silver nanoparticles for the mitigation of halotolerant sulphate-reducing bacteria, *J. Appl. Microbiol.*, 2019, **126**, 138–154.
51 J. Z. Barbosa, M. Hungria, S. A. Prior, M. C. Moura, G. Poggere and A. C. V. Motta, Improving yield and health of legume crops via co-inoculation with rhizobia and *Trichoderma*: A global meta-analysis, *Appl. Soil Ecol.*, 2022, **176**, 104493.
52 S. A. Saldaña, M. Sandra, P. Michelena and A. S. Palacios, *Trichoderma* as a biological control agent: mechanisms of action, benefits for crops and development of formulations, *World J. Microbiol. Biotechnol.*, 2023, **39**, 269.
53 R. Bansal, S. A. Sahoo, V. T. Barvkar, A. K. Srivastava and P. K. Mukherjee, *Trichoderma virens* exerts herbicidal effect on Arabidopsis thaliana via modulation of amino acid metabolism, *Plant Sci.*, 2023, **332**, 111702.
54 C. C. Castañeda-Casasola, M. F. Nieto-Jacobo, A. Soares, E. A. Padilla-Padilla, M. A. Anducho-Reyes, C. Brown, S. Soth, E. U. Esquivel-Naranjo, J. Hampton and A. Mendoza-Mendoza, Unveiling a microexon switch: Novel regulation of the activities of sugar assimilation and plant-cell-wall-degrading xylanses and cellulases by Xlr2 in *Trichoderma virens*, *Int. J. Mol. Sci.*, 2024, **25**, 5172.
55 B. A. Omran, M. Fazle, R. M. O. Abdel and K. H. Baek, Biogenically synthesized copper oxide, titanium oxide, and silver oxide nanoparticles: Characterization and biological effects, *Clean Technol. Environ. Policy*, 2024, DOI: **10.1007/s10098-024-02965-1**.
56 B. A. Omran, M. Fazle, M. O. Abdel-salam and K. Baek, Nanobiological synthesis of silver oxide-doped titanium oxide bionanocomposite targeting foodborne and phytopathogenic bacteria, *Food Biosci.*, 2024, **61**, 104790.
57 B. A. Omran, M. Fazle, R. M. O. Abdel and K. H. Baek, TrichogenicAg_2O/CuO Nanoalloys: Biomimetic synthesis, physicochemical characterization, and plausible

antibacterial mechanism, *Food Bioprocess Technol.*, 2025, **18**, 260–278.
58 S. Sahoo and J.-J. Shim, Facile synthesis of three-dimensional ternary $ZnCo_2O_4$/reduced graphene oxide/NiO composite film on nickel foam for next generation supercapacitor electrodes, *ACS Sustain. Chem. Eng.*, 2017, **5**, 241–251.
59 M. Ershadi, M. Javanbakht, S. Ahmad, D. Brandell, M. Lee and B. Zahiri, Facile stitching of graphene oxide nanosheets with ethylenediamine as three dimensional anode material for lithium-ion battery, *J. Alloys Compd.*, 2020, **818**, 152912.
60 R. Goyat, J. Singh, A. Umar, Y. Saharan, V. Kumar, H. Algadi, S. Akbar and S. Baskoutas, Modified low-temperature synthesis of graphene oxide nanosheets: Enhanced adsorption, antibacterial and antioxidant properties, *Environ. Res.*, 2022, **215**, 114245.
61 K. Cao, Z. Tian, X. Zhang, Y. Wang and Q. Zhu, Green preparation of graphene oxide nanosheets as adsorbent, *Sci. Rep.*, 2023, **13**, 9314.
62 B. A. Omran and K. H. Baek, Inhibition of foodborne bacterial pathogens using novel mycosynthesized cobalt nano ferrites and $CoFe_2O_4$ nanoparticles anchored on functionalized multi-walled carbon nanotube bionanocomposites, *J. Environ. Chem. Eng.*, 2023, **11**, 111465.
63 B. A. Omran and K. Baek, Dual extracellular mycofabrication of cobalt and zinc nano metal oxides mediated by mycelial-cell free filtrate of *Aspergillus sojae*: Characterization and assessment of antibacterial activity, *J. Mol. Struct.*, 2024, **1300**, 137190.
64 B. A. Omran, Inspired biological synthesis of nanomaterials using eukaryotic microbial nano-machinery, in *Nanobiotechnology: A Multidisciplinary Field of Science*, Springer, 2020, pp. 81–109.
65 Y. Liu, Y. Yang, E. Yuhan, C. Pang, D. Cui and A. Li, Insight into microbial synthesis of metal nanomaterials and their environmental applications: Exploration for enhanced controllable synthesis, *Chin. Chem. Lett.*, 2024, **35**, 109651.
66 P. Guzmán-Guzmán, E. Valencia-Cantero and G. Santoyo, Plant growth-promoting bacteria potentiate antifungal and plant-beneficial responses of *Trichoderma atroviride* by upregulating its effector functions, *PLoS One*, 2024, **19**, e0301139.
67 J. Zhang, W. Tang, Q. Huang, Y. Li and M. Wei, *Trichoderma*: A treasure house of structurally diverse secondary metabolites with medicinal importance, *Front. Microbiol.*, 2021, **12**, 1–21.
68 E. Priyadarshini, S. S. Priyadarshini, B. G. Cousins and N. Pradhan, Metal-Fungus interaction: Review on cellular processes underlying heavy metal detoxification and synthesis of metal nanoparticles, *Chemosphere*, 2021, **274**, 129976.
69 M. R. Rami, M. Meskini and B. E. Sharafabad, Fungal-mediated nanoparticles for industrial applications: synthesis and mechanism of action, *J. Infect. Public Health*, 2024, **17**, 102536.
70 J. Liu, S. Chen, Y. Liu and B. Zhao, Progress in preparation, characterization, surface functional modification of graphene oxide: A review, *J. Saudi Chem. Soc.*, 2022, **26**, 101560.
71 L. S. Sundar and M. W. Ashraf, Synthesis and characterization methods of graphene oxide nanomaterial for biomedical and toxicity applications: A comprehensive review, *Inorg. Chem. Commun.*, 2025, **174**, 113936.
72 B. A. Omran, B. S. Tseng and K.-H. Baek, Nanocomposites against *Pseudomonas aeruginosa* biofilms: Recent advances, challenges, and future prospects, *Microbiol. Res.*, 2024, **282**, 127656.
73 B. Thangaraj, P. R. Solomon, N. Wongyao, M. I. Helal, A. Abdullah, S. Abedrabbo and J. Hassan, Synthesis of reduced graphene oxide nanosheets from sugarcane dry leaves by two-stage pyrolysis for antibacterial activity, *Nano Mater. Sci.*, 2024, **6**, 625–634.
74 F. Kiani, N. A. Astani, R. Rahighi, A. Tayyebi, M. Tayebi, J. Khezri, E. Hashemi, U. Rothlisberger and A. Simchi, Effect of graphene oxide nanosheets on visible light-assisted antibacterial activity of vertically-aligned copper oxide nanowire arrays, *J. Colloid Interface Sci.*, 2018, **521**, 119–131.
75 M. Muqoyyanah, F. Khoerunnisa, M. Handayani, Y. D. Rahmayanti, H. A. Triadi, R. U. Annifah, Y. K. A. A. Iasya, T. Gunawan, W. W. Lestari, E. H. Sanjaya and W. D. Astuti, Effect of silver nanoparticles on the morphological, antibacterial activity and performance of graphene oxide-embedded polyvinylidene fluoride membrane, *J. Environ. Chem. Eng.*, 2023, **11**, 111394.
76 T. Tene, M. Guevara, F. B. Palacios, T. Paulina, M. Barrionuevo, C. V. Gomez and S. Bellucci, Optical properties of graphene oxide, *Front. Chem.*, 2023, **11**, 1214072.
77 N. Tahir, M. Zahid, A. Jillani, M. Yaseen, Q. Abbas, R. Abdul Shakoor and I. Shahid, Ternary silver tungstate-MoS_2/graphene oxide heterostructure nanocomposite for enhanced photocatalysis under visible light and antibacterial activity, *J. Photochem. Photobiol. A Chem.*, 2023, **436**, 114376.
78 J. Klein, L. Kampermann, B. Mockenhaupt, M. Behrens, J. Strunk and G. Bacher, Limitations of the Tauc plot method, *Adv. Funct. Mater.*, 2023, **33**, 2304523.
79 D. C. T. Nguyen, K.-Y. Cho and W.-C. Oh, Synthesis of frost-like CuO combined graphene-TiO_2 by self-assembly method and its high photocatalytic performance, *Appl. Surf. Sci.*, 2017, **412**, 252–261.
80 L. Gao, L. Wang, L. Yang, Y. Zhao, N. Shi, C. An, Y. Sun, J. Xie, H. Wang, Y. Song and Y. Ren, Preparation, characterization and antibacterial activity of silver nanoparticle/graphene oxide/diatomite composite, *Appl. Surf. Sci.*, 2019, **484**, 628–636.
81 R. Al-Gaashani, A. Najjar, Y. Zakaria, S. Mansour and M. A. Atieh, XPS and structural studies of high quality graphene oxide and reduced graphene oxide prepared by different chemical oxidation methods, *Ceram. Int.*, 2019, **45**, 14439–14448.
82 M. Maruthupandy, G. Rajivgandhi, T. Muneeswaran, M. Anand and F. Quero, Highly efficient antibacterial activity of graphene/chitosan/magnetite nanocomposites against ESBL-producing *Pseudomonas aeruginosa* and *Klebsiella pneumoniae*, *Colloids Surf., B*, 2021, **202**, 111690.

83 N. Minh, P. Ngoc, B. Long, D. Chau, U. Nhi, N. Nhat, L. Minh, L. Ngoc, H. Minh, M. Thanh and N. Huu, Synthesis of silver/reduced graphene oxide for antibacterial activity and catalytic reduction of organic dyes, *Synth. Met.*, 2020, **260**, 116260.
84 K. Kala, N. Padmasini, M. N. Harish, J. Shanmuga and R. Siranjeevi, A sustainable and highly efficient photocatalytic and supercapacitor electrode for biogenic nickel oxide nanoparticle infused graphene oxide, *Surf. Interfaces*, 2024, **49**, 104438.
85 N. M. Dat, D. B. Thinh, L. M. Huong, N. T. Tinh, N. T. T. Linh, N. D. Hai, N. D. Viet, N. T. Dat, M. T. Phong and N. H. Hieu, Facile synthesis and antibacterial activity of silver nanoparticles-modified graphene oxide hybrid material: the assessment, utilization, and anti-virus potentiality, *Mater. Today Chem.*, 2022, **23**, 100738.
86 L. S. Mokoena and J. P. Mofokeng, Synthesis and characterization of graphene oxide (GO) for the removal of lead ions in water, *Carbon Trends*, 2024, **15**, 100339.
87 P. Lakhani and C. K. Modi, Montmorillonite-silica-graphene oxide composite incorporating with chiral thiourea for the Strecker reaction, *Mol. Catal.*, 2024, **559**, 114080.
88 X. Song, L. Xie, M. Zhang, W. Wang, L. Li, X. Lu, P. Lei, D. Liu, Y. Chen, H. Chen and C. Zhao, Cu-decorated graphene oxide coatings with enhanced antibacterial activity for surface modification of implant, *Mater. Res. Bull.*, 2021, **141**, 111345.
89 N. M. Dat, P. N. B. Long, D. C. U. Nhi, N. N. Minh, L. M. Duy, L. N. Quan, H. M. Nam, M. T. Phong and N. H. Hieu, Synthesis of silver/reduced graphene oxide for antibacterial activity and catalytic reduction of organic dyes, *Synth. Met.*, 2020, **260**, 116260.
90 Y. Bu and B. S. Kim, Eco-friendly production of functionalized few-layer graphene using coffee waste extract and in-situ growth of copper oxide nanoparticles, *J. Environ. Chem. Eng.*, 2023, **11**, 109350.
91 S. Liu, D. Zhang, W. Chen, X. Wang, H. Ji, Y. Fu and C. Lü, Synthesis, antibacterial activity and action mechanism of silver-based nanomaterials with thermosensitive polymer-decorated graphene oxide as a stable support, *Mater. Today Commun.*, 2023, **36**, 106598.
92 T. Saha, M. Bin, N. Uddin, S. Quddus, M. Rahman and N. Sultana, Biogenic synthesis of copper oxide (CuO) NPs exploiting *Averrhoa carambola* leaf extract and its potential antibacterial activity, *Mater. Chem. Phys.*, 2023, **305**, 127979.
93 S. Zheng, W. W. Duley, P. Peng and Y. N. Zhou, Engineering intrinsic defects in CuO NWs through laser irradiation: Oxygen vs copper vacancies, *Appl. Surf. Sci.*, 2024, **642**, 158630.
94 B. S. Bharat and A. R. Babu, Iodine-doped reduced graphene oxide and titanium dioxide nanocomposite as effective amperometric glucose biosensor, *Mater. Chem. Phys.*, 2024, **320**, 129409.
95 E. Ceylan, O. Ozoglu, H. H. Ipekci, A. Tor and A. Uzunoglu, *Microchem. J.*, 2024, 110261.
96 Y. Wang, A. Abulizi, K. Okitsu and T. Ren, N-doped carbon-supported Cu–CuO nanoparticles for photocatalytic reduction of carbon dioxide, *Opt. Mater.*, 2024, **151**, 115360.
97 S. C. Vanithakumari, G. Jena, S. Sofia, C. Thinaharan, R. P. George and J. Philip, Fabrication of superhydrophobic titanium surfaces with superior antibacterial properties using graphene oxide and silanized silica nanoparticles, *Surf. Coatings Technol.*, 2020, **400**, 126074.
98 Y.-C. Chiang and T.-L. Tseng, Characterization and electrochemical properties of Pt nanoparticles deposited on titanium oxide nanofibers, *Mater. Chem. Phys.*, 2021, **267**, 124700.
99 J. Zeng, J. Zhuang, T. He, Q. Chen and Y. Liu, Microstructure and dielectric response of Mg doped $Cu_3Ti_2Ta_2O_{12}$ ceramics, *J. Mater. Sci.: Mater. Electron.*, 2019, **30**, 2652–2658.
100 M. Saffari, Z. H. Kavousi, M. Ghorbanloo, A. A. Nada, M. F. Bekheet, D. Bezzerga, J. Hong, A. Morsali, Y. Holade and R. Viter, Copper benzene-1,3,5-tricarboxylate based metal organic framework (MOF) derived CuO/TiO_2 nanofibers and their use as visible light active photocatalyst for the hydrogen production, *Appl. Surf. Sci.*, 2024, **678**, 161061.
101 A. P. Najafabadi, M. Pourmadadi, F. Yazdian, H. Rashedi, A. Rahdar and A. M. Díez-Pascual, pH-sensitive ameliorated quercetin delivery using graphene oxide nanocarriers coated with potential anticancer gelatin-polyvinylpyrrolidone nanoemulsion with bitter almond oil, *J. Drug Delivery Sci. Technol.*, 2023, **82**, 104339.
102 E. B. Noruzi, B. Shaabani, R. Eivazzadeh-Keihan and H. A. M. Aliabadi, Fabrication and investigation of a pentamerous composite based on calix[4]arene functionalized graphene oxide grafted with silk fibroin, cobalt ferrite, and alginate, *Int. J. Biol. Macromol.*, 2024, **259**, 129385.
103 L. M. Al-Harbi, W. S. Mohamed, A. A. Ebnalwaled, A. H. Said and M. Ezzeldien, The effect of synthesis conditions on the photokilling activity of TiO_2 nanostructures, *Mater. Res. Express*, 2023, **10**, 015004.
104 M. A. Khan, N. Nayan Shadiullah, M. K. Ahmad, S. C. Fhong, M. Tahir, R. A. Mohamed Ali and M. S. Mohamed Ali, Advanced nanoscale surface characterization of CuO nanoflowers for significant enhancement of catalytic properties, *Molecules*, 2021, **26**, 2700.
105 Y. Fan, Z. Ma, Y. Zhang, Y. Wang, Y. Ding, C. Wang and S. Cao, Sulfur-containing compounds from endophytic fungi: sources, structures and bioactivities, *J. Fungi*, 2022, **8**, 628.
106 N. Belachew, M. H. Kahsay, A. Tadesse and K. Basavaiah, Green synthesis of reduced graphene oxide grafted Ag/ZnO for photocatalytic abatement of methylene blue and antibacterial activities, *J. Environ. Chem. Eng.*, 2020, **8**, 104106.
107 Z. O. Alafif, M. Anjum, R. Kumar, S. M. Abdelbasir and M. A. Barakat, Synthesis of CuO–GO/TiO_2 visible light photocatalyst for 2-chlorophenol degradation, pretreatment of dairy wastewater and aerobic digestion, *Appl. Nanosci.*, 2019, **9**, 579–591.
108 A. A. Menazea and M. K. Ahmed, Synthesis and antibacterial activity of graphene oxide decorated by silver and copper oxide nanoparticles, *J. Mol. Struct.*, 2020, **1218**, 128536.

109 P. Fardinpour, H. Ghafouri and M. Reza, Facile green synthesis of graphene oxide/copper oxide nanocomposites using ginger essential oil and its enhanced antibacterial properties, *Mater. Sci. Eng. B*, 2024, **300**, 117100.
110 A. Umairah, N. Najmi, M. Ad, N. Dalila, N. Affandi, H. Al, M. Khouj, F. Nur, A. Mohd and N. Mohammad, Graphene oxide nanoparticles synthesized from waste tires: A multifaceted analysis of structure, morphology and antibacterial behavior, *Nano-Struct. Nano-Objects*, 2024, **38**, 101176.
111 K. Khalid, A. Zahra, U. Amara, M. Khalid, M. Hanif, M. Aziz, K. Mahmood, M. Ajmal, M. Asif, K. Saeed, M. F. Qayyum and W. Abbas, Titanium doped cobalt ferrite fabricated graphene oxide nanocomposite for efficient photocatalytic and antibacterial activities, *Chemosphere*, 2023, **338**, 139531.
112 R. M. Abdelhameed, O. M. Darwesh and M. El-shahat, Titanium-based metal-organic framework capsulated with magnetic nanoparticles: Antimicrobial and photocatalytic degradation of pesticides, *Microporous Mesoporous Mater.*, 2023, **354**, 112543.
113 M. Dhanalakshmi and V. Losetty, Investigation of antibacterial, antioxidant, cytotoxicity and photocatalytic dye degradation activity of green synthesized copper oxide nanoparticles using *Ceropegia debilis* plant extract, *Clean Technol. Environ. Policy*, 2024, DOI: **10.1007/s10098-024-02776-4**.
114 M. Woźniak-Budych, U. Zgórzyńska, L. Przysiecka, K. Załęski, M. Jarek, M. Jancelewicz, A. Domke, I. Iatsunskyi, G. Nowaczyk and K. Staszak, Copper oxide (I) nanoparticle-modified cellulose acetate membranes with enhanced antibacterial and antifouling properties, *Environ. Res.*, 2024, **252**, 119068.
115 A. Ojha, S. Thakur and J. Prakash, Graphene family nanomaterials as emerging sole layered nanomaterials for wastewater treatment: Recent developments, potential hazards, prevention and future prospects, *Environ. Adv.*, 2023, **13**, 100402.
116 A. Badoni and J. Prakash, Noble metal nanoparticles and graphene oxide based hybrid nanostructures for antibacterial applications: Recent advances, synergistic antibacterial activities, and mechanistic approaches, *Micro Nano Eng.*, 2024, **22**, 100239.
117 H. Zheng, R. Ma, M. Gao, X. Tian, Y. Li, L. Zeng and R. Li, Antibacterial applications of graphene oxides: Structure-activity relationships, molecular initiating events and biosafety, *Sci. Bull.*, 2018, **63**, 133–142.
118 L. Sun, D. Yu, L. Yang, F. Jia, Z. Juan, Y. Wang, Y. Wang, M. J. Kipper, L. Huang and J. Tang, Improvements in multifunctional graphene oxide-based separation membranes: Mechanism, modification and properties, *Mater. Today Commun.*, 2022, **33**, 104274.
119 I. M. J. Ng and S. Shamsi, Graphene oxide (GO): A promising nanomaterial against infectious diseases caused by multidrug-resistant bacteria, *Int. J. Mol. Sci.*, 2022, **23**, 9096.
120 S. Patil, C. Rajkuberan and S. Sagadevan, Recent biomedical advancements in graphene oxide and future perspectives, *J. Drug Delivery Sci. Technol.*, 2023, **86**, 104737.
121 T. Pulingam, K. Lin, J. Nelson, C. Wei and B. Fen, Mechanistic actions and contributing factors affecting the antibacterial property and cytotoxicity of graphene oxide, *Chemosphere*, 2021, **281**, 130739.
122 B. Omran and K.-H. Baek, Graphene-derived antibacterial nanocomposites for water disinfection: Current and future perspectives, *Environ. Pollut.*, 2022, **298**, 118836.
123 S. Panda, T. K. Rout, A. D. Prusty, P. M. Ajayan and S. Nayak, Electron transfer directed antibacterial properties of graphene oxide on metals, *Adv. Mater.*, 2018, **30**, 1702149.
124 M. Ma, Y. Wu, J. Song, Y. Li, L. Sun and Y. Xiao, *Food Control*, 2025, **174**, 111267.
125 D. Crnčević, L. Krce, Z. Brkljača, M. Cvitković, S. B. Brčić, R. Čož-Rakovac, R. Odžak and M. Šprung, *RSC Adv.*, 2025, **15**, 1490–1506.
126 R. R. Varma, J. G. Pandya, F. U. Vaidya, C. Pathak, B. S. Bhatt and M. N. Patel, *Chem. – Biol. Interact.*, 2020, **330**, 109231.
127 Z. Khanjari, E. Chamani, K. Heydaryan, Z. M. Mizwari, F. Salmani, A. R. Farimani, M. Siami-Aliabad, Z. Kiani, P. Mohammadparast-Tabas and S. Mortazavi-Derazkola, *Mater. Today Commun.*, 2024, **39**, 109214.
128 K. Gangwar and P. Jeevanandam, Synthesis of SnO_2-Ag nanocomposites *via* thermal decomposition method and their application for catalytic reduction of 4-nitrophenol and photocatalytic degradation of congo red, *J. Mol. Struct.*, 2023, **1285**, 135423.
129 G. F. Aaga and S. T. Anshebo, Green synthesis of highly efficient and stable copper oxide nanoparticles using an aqueous seed extract of *Moringa stenopetala* for sunlight-assisted catalytic degradation of Congo red and alizarin red, *Heliyon*, 2023, **9**, e16067.
130 M. Rashad, S. Helali, N. M. Shaalan, A. E. Albalawi, N. S. Alatawi, B. Al-Faqiri, M. M. Al-Belwi and A. M. Alsharari, Dual studies of photo degradation and adsorptions of Congo red in wastewater on graphene–copper oxide heterostructures, *Materials*, 2023, **16**, 3721.
131 P. B. Sreelekshmi, R. R. Pillai, B. Binish and A. P. Meera, Enhanced photocatalytic degradation of malachite green using highly efficient copper oxide/graphene oxide nanocomposites, *Top. Catal.*, 2022, **65**, 1885–1898.
132 Y. Yang, N. Ali, A. Khan, S. Khan, S. Khan, H. Khan, S. Xiaoqi, W. Ahmad, S. Uddin and N. Ali, Chitosan-capped ternary metal selenide nanocatalysts for efficient degradation of Congo red dye in sunlight irradiation, *Int. J. Biol. Macromol.*, 2021, **167**, 169–181.
133 H. Liu, N. Gao, L. Wang and D. He, Ceramic membrane supported with CuO for catalytic degradation of azo dyes using sulfate radicals, *J. Mater. Sci.*, 2023, **58**, 17442–17458.
134 L. Rao, Y. Yang, L. Chen, X. Liu, H. Chen, Y. Yao and W. Wang, Highly efficient removal of organic pollutants via a green catalytic oxidation system based on sodium metaborate and peroxymonosulfate, *Chemosphere*, 2020, **238**, 124687.
135 N. T. Dung, T. T. Trang, V. D. Thao, T. V. Thu, N. Q. Tung and N. N. Huy, Enhanced degradation of organic dyes by peroxymonosulfate with Fe_3O_4-$CoCO_3$/rGO hybrid

activation: A comprehensive study, *J. Taiwan Inst. Chem. Eng.*, 2022, **133**, 104279.

136 C. Tan, N. Gao, Y. Deng, J. Deng, S. Zhou, J. Li and X. Xin, Radical induced degradation of acetaminophen with Fe_3O_4 magnetic nanoparticles as heterogeneous activator of peroxymonosulfate, *J. Hazard. Mater.*, 2014, **276**, 452–460.

137 X. Dai, Z. Liu, J. Wang, K. Zhang, D. Ma, W. Chen and H. Zheng, Bimetallic CuMo@TiO_2 activating peroxymonosulfate for micropollutants degradation: Synergy and mechanism, *J. Environ. Chem. Eng.*, 2023, **11**, 109304.

138 J. Wei, F. Li, L. Zhou, D. Han and J. Gong, Strategies for enhancing peroxymonosulfate activation by heterogenous metal-based catalysis: A review, *Chinese J. Chem. Eng.*, 2022, **50**, 12–28.

139 M. Kohantorabi, G. Moussavi and S. Giannakis, A review of the innovations in metal-and carbon-based catalysts explored for heterogeneous peroxymonosulfate (PMS) activation, with focus on radical *vs.* non-radical degradation pathways of organic contaminants, *Chem. Eng. J.*, 2020, **411**, 127957.

140 F. Ghanbari and M. Moradi, Application of peroxymonosulfate and its activation methods for degradation of environmental organic pollutants, *Chem. Eng. J.*, 2017, **310**, 41–62.